https://doi.org/10.5194/egusphere-2026-3109
Preprint. Discussion started: 13 July 2026

Evaluation of area-source methane-emission quantification by Uncrewed Aerial Systems using Gauss's law

Kevin S. Rozmiarek[1,2], Elijah A. Miller[3], Irina Overeem[1,2], Gregory B. Rieker[3], and Tyler R. Jones[1]

[1]Institute of Arctic and Alpine Research, University of Colorado Boulder, Boulder, CO, USA
[2]Department of Geological Sciences, University of Colorado Boulder, Boulder, CO, USA
[3]Precision Laser Diagnostics Laboratory, University of Colorado Boulder, Boulder, CO, USA

Correspondence: Kevin S. Rozmiarek (Kevin.Rozmiarek@colorado.edu)

Abstract. Quantifying methane emissions from lakes and wetlands remains a persistent challenge. Existing measurement approaches commonly sample only at distinct points (chambers) or integrate over poorly defined and meteorology-dependent footprints (eddy covariance, flux-gradient methods). A different framework for methane-flux estimation from lakes and wetlands entails an aerial cylindrical mass-balance technique in which an aircraft with methane and wind sensors circumscribes a methane source. This creates a control volume, allowing for the enclosed flux to be determined with Gauss's divergence theorem. The suitability of this methodology has not been evaluated for uncrewed aerial systems (UAS). We conducted an observing system simulation experiment (OSSE) that coupled a Gaussian-plume forward model with a simulated Gaussian cylindrical-flux estimation over an idealized methane-emitting lake. Across three experiments, we tested the effects of (i) receptor (points of collocated methane and wind measurements) grid resolution, (ii) methane contamination from a nearby upwind lake, and (iii) the effects of sampling under evolving atmospheric stability, on retrieval accuracy and precision. We introduce nondimensional variables to represent the estimation error from these three effects for a broader set of system configurations. Vertical-receptor resolution was the dominant control on retrieval accuracy, while azimuthal resolution primarily affected precision relative to the vertical resolution. When a nearby lake (~0.1–10 km) with an upwind-methane source was introduced to the simulation, this induced a systematic negative bias compared to the true methane flux. Under prescribed atmospheric-stability transitions, retrieval accuracy degraded monotonically with increased mission duration, with the shortest flights (30 min) preserving the highest flux retrieval accuracy across all stability transitions tested. This is because shorter flights more closely capture a snapshot of the environment before changes in the atmosphere can occur, which can skew methane-flux estimates. However, repeating short flights and averaging the resulting source-flux retrievals improved precision over single flights even across longer (12 h) atmospheric stability transitions. Within our nondimensional framework, signal-to-noise increased retrieval accuracy, but by an amount that was determined by the geometry of the measured lake and observations. The OSSE framework presented here provides a quantitative basis for planning UAS methane-flux-measurement campaigns using cylindrical mass-balance over lakes, wetlands, and possibly other heterogeneous natural methane sources.

https://doi.org/10.5194/egusphere-2026-3109
Preprint. Discussion started: 13 July 2026

1 Introduction

Methane (CH_4) is a major contributor to anthropogenic climate forcing and has accounted for 20% of observed warming since pre-industrial times (Kirschke et al., 2013; Masson-Delmotte et al., 2021). A diverse array of sources contributes to atmospheric methane, including natural emissions (e.g., wetlands, lakes, pyrogenic sources, termites), anthropogenic emissions (e.g., rice cultivation, ruminant livestock, oil and gas extraction, waste management), and feedback-driven emissions such as permafrost thaw (Lan et al., 2021; Saunois et al., 2025). These sources differ markedly in magnitude, temporal dynamics, and spatial extent. (Räsänen et al., 2021; Riquelme del Rio et al., 2024; Saunois et al., 2025; Allen et al., 2025). This poses a challenge for accurately quantifying and modeling methane fluxes across source categories and reconciling bottom-up (e.g., chamber fluxes at ground level or process-based models) and top-down (e.g., atmospheric inversions) estimates (Desjardins et al., 2018; Helmig and Caputi, 2025; Zhu et al., 2025; Basso et al., 2026). For example, measurement approaches optimized for confined settings with high methane concentrations, such as enclosure chambers in livestock facilities or surface flux chambers, are poorly transferable to spatially diffuse area sources (e.g., lakes and wetlands) which result in low methane concentrations (Hristov et al., 2018; Rodríguez-García et al., 2023). Reconciling methane-flux estimation across scales demands a suite of measurement technologies and conceptual frameworks capable of bridging e.g., point-scale, ecosystem-scale, and regional-scale flux estimation. Despite substantial methodological advances on this front, significant gaps remain in our ability to accurately quantify methane fluxes across the full diversity of source types and environments (Malone et al., 2021; Allen et al., 2025).

Lakes and natural wetlands rank among the largest natural sources of the global atmospheric methane budget where bottom-up estimates report $248[159-369]\,\mathrm{Tg\,CH_4\,yr^{-1}}$, or 37% of the global emissions (Saunois et al., 2025). Lakes and wetlands produce methane due to persistently high-water saturation that generates anoxic conditions necessary to sustain methanogenic-microbial communities (Bridgham et al., 2013). These natural systems have methane fluxes than span several orders of magnitude, $0-10^3\,\mathrm{mg\,CH_4\,m^{-2}\,d^{-1}}$ (Ortiz-Llorente and Alvarez-Cobelas, 2012). Critically, wetland landscapes often comprise mosaics of inundated wetland, drier upland soils, open water bodies (including lakes and ponds), forested areas, and other land cover types (Lehner and Döll, 2004; Olefeldt et al., 2021). This environmental heterogeneity occurs on spatial scales that are comparable to, or smaller than, the footprints of many atmospheric trace-gas flux methods, posing a fundamental challenge for estimating both fine-scale and regional methane fluxes.

At the small spatial scale, chamber measurements capture surface–atmosphere flux at discrete points (Hutchinson and Mosier, 1981; Rodríguez-García et al., 2023). Chamber flux measurements on shallow-lake shorelines or within individual wetlands often vary by orders of magnitude over distances of only a few meters, f.e. driven by peat or organic horizon depth (Köster et al., 2017), hydrological connectivity (Rey-Sanchez et al., 2019), local energy balance (Yvon-Durocher et al., 2014; He et al., 2025), and variability in subsurface methanogen-community structure (Arnold et al., 2023; Rozmiarek et al., 2025). This extreme flux variability makes upscaling from discrete points to landscape-scale (~1–100 km^2) problematic and has led to widely varying empirical upscaling schemes (Forbrich et al., 2024; Zhu et al., 2025). Currently, there is little consensus on the sampling techniques required for robust landscape-scale flux estimates.

https://doi.org/10.5194/egusphere-2026-3109
Preprint. Discussion started: 13 July 2026

Eddy covariance (EC) has proven effective in providing continuous, local-scale methane flux estimates over lakes and wetlands (~0.01 to 1 km^2), by correlating high-frequency vertical wind fluctuations with methane concentration to resolve turbulent exchange (Aubinet et al., 2012; Feron et al., 2024). However, eddy-covariance fluxes are associated with dynamic and meteorology-dependent spatial footprints that vary with wind direction, wind speed, and atmospheric stability, often extending beyond the nominal wetland or lake into adjacent land covers (Matthes et al., 2014). In heterogeneous lake and wetland mosaics, or for small water bodies, the complex and time-varying EC flux footprint complicates unambiguous attribution of measured fluxes to specific methane-emitting surfaces and processes (Metzger, 2018).

Airborne measurement platforms, including crewed aircraft and uncrewed aerial systems (UAS, i.e. drones), extend the accessible spatial domain for methane-flux estimation, while providing additional flexibility in sampling geometry. There are multiple options for airborne flux estimation. 1) *Downward-pointing spectrometry methods* employ passive imaging spectrometers or active laser-based retrievals. Passive spectral retrievals may be limited by surface albedo constraints over open water (Elder et al., 2020), while active systems offer improved performance but are currently limited to crewed aircraft (Barton-Grimley et al., 2022). 2) *Flux-gradient methods* estimate vertical turbulent flux from the product of the vertical concentration gradient and an inferred eddy diffusivity (Maier and Schack-Kirchner, 2014) but remain sensitive to footprint attribution. This challenge intensifies at higher flight altitudes as enhanced atmospheric mixing integrates emissions over progressively larger areas. 3) *Flux-plane methods* integrate the downwind-methane flux through a vertical curtain (plane) oriented perpendicular to the mean wind (Barkley et al., 2017; Mohammadloo et al., 2025). Such approaches partially circumvent footprint ambiguity but introduce two additional complications: the requirement to accurately characterize a background-methane concentration against which fluxes are measured, and the need to fully capture the lateral and vertical extent of the plume during sampling. To date, these methods have been applied to point-source anthropogenic sources (e.g., smokestacks, natural gas infrastructure leaks, (France et al., 2021; Mohammadloo et al., 2025) and to landscape-scale such as wetlands (~1–1,000 km^2, Barker et al. (2021)). Their suitability for small (~0.01–10 km^2) area sources such as lakes and individual areas of inundation within wetlands is not well established.

Conley et al. (2017) introduced an aerial mass-balance approach in which a cylindrical atmospheric control volume is established above a methane point source. Measurements taken on the cylindrical atmospheric control volume are similar to those of flux-plane methods but distributed azimuthally around a methane source. The Conley et al. (2017) method (hereafter the *cylindrical-flux method*) applies Gauss's divergence theorem to relate an unknown surface emission to the net flux through the lateral surface of the cylinder. Sampling both upwind and downwind sectors on the cylinder inherently removes the need to quantify background concentrations (Conley et al., 2017). The *cylindrical-flux method* offers key advantages for heterogeneous area sources such as lake and wetland mosaics. Unlike flux-gradient and flux-plane techniques, the cylindrical-flux method explicitly bounds a finite control volume and simultaneously characterizes background methane mole fraction. However, the performance of cylindrical mass-balance retrievals has been demonstrated only for high-emission point sources to date. Whether the approach holds for area sources such as lakes, nearby contaminating sources outside the control volume, or UAS platforms operating under transient boundary-layer conditions remains largely untested.

https://doi.org/10.5194/egusphere-2026-3109
Preprint. Discussion started: 13 July 2026

To evaluate the feasibility and accuracy of the *cylindrical-flux method* for methane emissions from lakes, we conduct an observing system simulation experiment (OSSE) that couples a forward representation of methane dispersion over an idealized circular lake with a Gaussian cylindrical flux retrieval. In this OSSE, we prescribe a lake-averaged methane flux and simulate a resulting atmospheric plume under idealized, yet meteorologically realistic conditions. We emulate UAS sampling on a cylinder surrounding a lake and apply the cylindrical-flux method to retrieve the lake-integrated flux (Conley et al., 2017). We systematically quantify the accuracy and precision of lake-flux retrieval by exploring three effects: (1) the spatial and temporal resolution of sampling, (2) contamination from downwind area sources outside the control volume, and (3) plume perturbations due to atmospheric transience. We then abstract varying system configurations with nondimensional variables to make error approximation generalizable to different system configurations. These analyses yield quantitative guidance for designing UAS missions that seek to retrieve area-integrated methane fluxes from lakes and other heterogeneous area sources using the *cylindrical-flux method.*

2 Methods

The OSSE couples a forward plume model with an inverse retrieval which simulates the act of measuring the plume. The OSSE forward component used a Gaussian-plume model to generate synthetic methane concentration fields over an idealized circular lake. In the measurement simulation, these fields are sampled at discrete points on a surrounding cylinder wall, emulating an orbiting UAS performing measurements of methane mole fraction with wind velocity and direction at the cylindrical boundary (Fig. 1). A mass-balance retrieval (Conley et al., 2017) then recovers the prescribed lake flux from those simulated measurements. Across our three experiments, we use a common lake geometry, plume dispersion parameterization, model for synthetic sensor measurements, and retrieval method. Experiments differ only in the atmospheric states applied in the forward model and the receptor (points of collocated methane and wind measurements) spatial and temporal configuration in the retrieval. The following subsections describe each component of the OSSE framework and then present the design of each experiment.

2.1 Cylindrical mass-balance flux retrieval

2.1.1 Derivation from the scalar continuity equation

The cylindrical mass-balance retrieval follows the approach introduced by Conley et al. (2017) for aircraft-based methane-source quantification and is adapted here for application to area sources sampled by UAS. We begin with the integral form of the scalar budget equation for a passive, conservative tracer with mass concentration c in a turbulent flow field $\mathbf{u} = u\hat{\mathbf{i}} + v\hat{\mathbf{j}} + w\hat{\mathbf{k}}$. For a fixed control volume V, the budget takes the form:

$$Q_c = \langle \frac{\partial m}{\partial t} \rangle + \iiint_V \nabla \cdot (c\mathbf{u})\, dV, \tag{1}$$

https://doi.org/10.5194/egusphere-2026-3109
Preprint. Discussion started: 13 July 2026

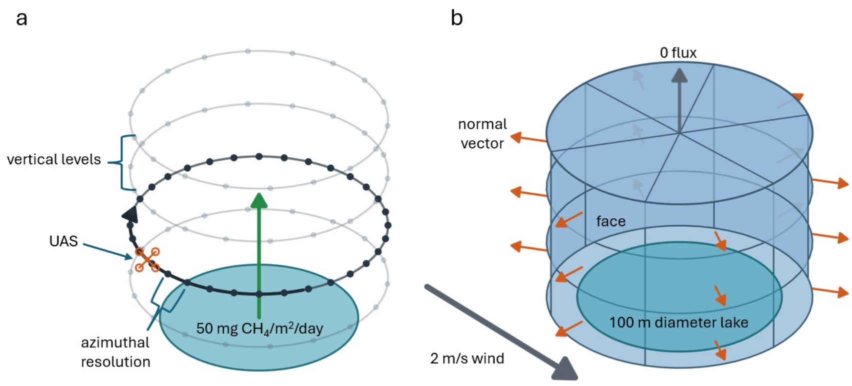

Figure 1. Conceptual diagram for the *cylindrical-flux method*. (a) Top-down schematic of the target lake and the cylindrical measurement ring used in the method. The blue disk represents the lake surface, the dark circular outline marks the lateral control surface, and points show discrete receptor locations sampled around the ring. The curved arrow indicates the azimuthal sampling direction and highlights that the continuous control surface is approximated by finite angular sampling. (b) Isometric schematic of the cylindrical sampling geometry surrounding the lake. Stacked receptor rings represent measurements at multiple heights along the lateral control surface. The green vertical arrow represents the lake-to-atmosphere methane flux being inferred from the measured concentration and wind field on the surrounding control surface. (c) Schematic of the cylindrical control volume used to convert measured methane enhancements and winds into a lake-scale flux estimate. The lateral surface is divided into azimuth-height receptor cells with a top cap to illustrate numerical integration over the control-volume boundary. Orange arrows show outward-facing lateral surface normals used to compute advective flux through each face; gray arrows indicate the wind/transport direction.

where Q_c is the net source of the tracer within V (here, the lake surface methane flux integrated over the lake area), $\langle \partial m/\partial t \rangle$ is the time rate of change of the total tracer mass m within the volume, and the volume integral represents the total flux divergence of $c\mathbf{u}$ within V. The scalar flux divergence can be decomposed into two terms:

$$\nabla \cdot (c\mathbf{u}) = \mathbf{u} \cdot \nabla c + c \nabla \cdot \mathbf{u}. \tag{2}$$

The first term on the right-hand side represents advection of the scalar gradient by the wind, while the second is proportional to the horizontal wind divergence. Conley et al. (2017) performed a scale analysis of advection and divergence using typical convective boundary-layer parameters and showed that the divergence term is at least an order of magnitude smaller than the gradient term for all but the weakest sources at low wind speeds (their Fig. 2), scaling as D/L where D is the magnitude of the horizontal divergence and L is the characteristic plume length scale. In Experiment 2, we will explicitly test the effect of the divergence term by introducing a contaminating plume not included in their framework.

We apply a Reynolds decomposition to the scalar field. Following Conley et al. (2017), we write $c = C + c'$, where C is the mean concentration around a closed flight loop at a given altitude and c' is the departure from that loop mean. Subtract-

https://doi.org/10.5194/egusphere-2026-3109
Preprint. Discussion started: 13 July 2026

ing the loop-mean concentration does not alter the gradient term, because $\nabla C = 0$ around any closed path. Substituting this decomposition into Eq. (2) yields:

$$\mathbf{u}_h \cdot \nabla c + c \nabla \cdot \mathbf{u}_h = \mathbf{u}_h \cdot \nabla c' \tag{3}$$

where $\mathbf{u}_h = u\hat{\mathbf{i}} + v\hat{\mathbf{j}}$ is the horizontal wind vector. The volume integral in Eq. (1) therefore simplifies to $\iiint_V \nabla \cdot (c'\,\mathbf{u})\,dV$.

We now apply Gauss's divergence theorem to convert this volume integral to a surface integral over the closed surface S bounding V:

$$Q_c = \langle \frac{\partial m}{\partial t} \rangle + \iiint\limits_V \nabla \cdot (c'\,\mathbf{u})\,dV = \langle \frac{\partial m}{\partial t} \rangle + \oint\limits_S c'\,\mathbf{u} \cdot \hat{\mathbf{n}}\,dS \tag{4}$$

where $\hat{\mathbf{n}}$ is the outward-pointing unit normal on S. In our cylindrical scheme, the surface S can be decomposed into three elements: the ground surface at $z = 0$ (through which Q_c is emitted and through which no other significant flux enters or leaves), the lateral cylindrical wall, and a horizontal cap at $z = z_{\max}$. If the cylinder extends sufficiently above the plume that no tracer flux crosses the cap, the surface integral reduces to a lateral integral only:

$$\oint\limits_S c'\,\mathbf{u} \cdot \hat{\mathbf{n}}\,dS = \int\limits_0^{z_{\max}} \oint\limits_l c'\,\mathbf{u}_h \cdot \hat{\mathbf{n}}\,dl\,dz \tag{5}$$

where l is the closed flight path at each altitude. Combining Eqs. (4) and (5), we obtain the working equation for the cylindrical mass-balance retrieval:

$$Q_c = \langle \frac{\partial m}{\partial t} \rangle + \int\limits_0^{z_{\max}} \oint\limits_l c'\,\mathbf{u}_h \cdot \hat{\mathbf{n}}\,dl\,dz. \tag{6}$$

Along each closed path, the instantaneous outward horizontal flux of the concentration is computed and integrated around the loop; summing these loop integrals over the altitude range yields the total horizontal flux divergence via Gauss's theorem. The storage term $\langle \partial m/\partial t \rangle$ represents the time rate of change of tracer mass within the cylinder.

In the present study, we make the quasi-steady approximation $\langle \partial m/\partial t \rangle \approx 0$ and assume that the vertical flux through the cylinder cap is zero, so that Eq. (6) reduces to a balance between the surface source and the net lateral advective flux of the concentration perturbation:

$$\iint\limits_{A_{\text{lake}}} F_{\text{surface}}\,dA \approx \int\limits_0^{z_{\max}} \oint\limits_l c'\,\mathbf{u}_h \cdot \hat{\mathbf{n}}\,dl\,dz \tag{7}$$

https://doi.org/10.5194/egusphere-2026-3109
Preprint. Discussion started: 13 July 2026

where F_{surface} is the (in general spatially varying) surface methane flux; the spatially uniform value F_0 prescribed in our experiments (Sect. 2.1.3) is the special case $F_{\text{surface}} \equiv F_0$. Equation (7) states that the area-integrated lake emission equals the net outward horizontal flux of methane enhancement through the lateral surface of the enclosing cylinder. This formulation inherently resolves the ambient background concentration, because the upwind sector of the cylinder, where $c' < 0$ relative to the loop mean, contributes negative flux that offsets the enhanced downwind sector, yielding a net lateral flux proportional only to the internal source.

2.1.2 Discrete quadrature on the cylindrical control surface

In practice, the continuous lateral integral in Eq. (4) is approximated by a finite set of receptor positions distributed as cells on the outer cylindrical surface. Receptors are the location of both methane and wind measurement and may be interpreted as the average measurement values of a traveling UAS along the receptor cell. Receptors are placed on a single ring of radius R_{outer} centered on the lake at discrete azimuthal positions θ_j and repeated at height levels z_k. The discrete lateral cell area element represented by the receptor at position (j,k) is

$$\Delta A_{j,k} = R_{\text{outer}}\,\Delta\theta\,\Delta z_k \tag{8}$$

where $\Delta\theta = 2\pi/n_{\text{az}}$ is the uniform azimuthal spacing and Δz_k is the height-band thickness assigned to level k by a midpoint rule. Under this rule, the lowest height band extends from the surface to the midpoint between the first and second receptor levels, and the uppermost band is mirrored symmetrically above the highest receptor, so that the full column from the surface to the cylinder top is partitioned without gaps.

The discrete lateral mass flux is then accumulated as

$$Q_{\text{lat}} = \sum_j \sum_k \rho_{c,j,k}\, v_{r,j}\, \Delta A_{j,k} \tag{9}$$

where $\rho_{c,j,k}$ is the methane mass concentration at receptor (j,k), obtained by converting the measured mole fraction (in ppb) to mass concentration using the local air density and molar masses and $v_{r,j} = U_j \cos(\theta_j - \text{wd}_{\text{to}})$ is the outward radial component of the horizontal wind. The retrieved lake-mean surface flux thus

$$F_{\text{ret}} = \frac{Q_{\text{lat}}}{A_{\text{lake}}} \tag{10}$$

where F_{ret} is reported in $\text{mg}\,\text{CH}_4\,\text{m}^{-2}\,\text{d}^{-1}$.

2.1.3 Control volume geometry

All experiments used the same idealized lake and control volume configuration. The target lake was represented as a flat circular disk of diameter 100 m ($r_{\text{lake}} = 50$ m). The outer receptor ring was placed 10 m beyond the lake edge ensuring that the receptor

https://doi.org/10.5194/egusphere-2026-3109
Preprint. Discussion started: 13 July 2026

ring fully encloses the source while maintaining a practically achievable proximity for UAS operations. In temperate lakes, this is an appropriate choice. In boreal and Arctic lakes however, care should be taken as methane emissions are known to persist radially outwards from a lake's margin (Elder et al., 2020). Receptor positions are defined in a meteorological azimuth convention relative to the lake center (0° = north, 90° = east).

The prescribed lake-mean methane flux was spatially and temporally uniform at $F_0 = 50\,\mathrm{mg\,CH_4\,m^{-2}\,d^{-1}}$, a value representative of moderately productive boreal and temperate lakes (Bastviken et al., 2011). This uniform-flux formulation represents a lake-mean effective surface emission rather than explicitly resolving sub-lake heterogeneity due to littoral enhancement or ebullition hotspots.

2.2 Gaussian plume forward model

2.2.1 Point-source kernel

Synthetic methane concentration fields were generated using a Gaussian plume model. For a ground-level point source with perfect ground reflection, the steady-state concentration enhancement at a receptor located at downwind distance x_d, crosswind distance y_c, and height z is

$$C(x_d, y_c, z) = \frac{Q}{\pi\,\sigma_y(x_d)\,\sigma_z(x_d)\,U}\exp\left(-\frac{y_c^2}{2\sigma_y^2}\right)\exp\left(-\frac{z^2}{2\sigma_z^2}\right) \tag{11}$$

where Q is the emission rate, U is the reference wind speed used in plume dilution, and σ_y and σ_z are the lateral and vertical dispersion coefficients, respectively.

The Gaussian plume model was chosen because it provides a smooth, analytically tractable concentration field against which the inverse retrieval can be tested under controlled conditions. The purpose of the OSSE is to probe the sensitivity of the retrieval to sampling geometry, atmospheric stability, and contamination, not to reproduce the structure of real turbulent plumes. For these objectives, the Gaussian plume is a well-understood forward model (Pasquill and Smith, 1983).

2.2.2 Dispersion parameterization

Lateral and vertical dispersion were parameterized using the Pasquill–Gifford classification with Briggs rural dispersion coefficients (Briggs, 1973; Turner, 2020):

$$\sigma_y(x) = \frac{a_y\,x}{\sqrt{1 + b_y\,x}} \tag{12}$$

$$\sigma_z(x) = a_z\,x\,(1 + b_z\,x)^{p_z} \tag{13}$$

where the coefficients a_y, b_y, a_z, b_z, and p_z are specific to each Pasquill stability class. The Briggs rural parameterization was selected as appropriate for the open-terrain, low-roughness environment surrounding a lake. Four stability classes were

https://doi.org/10.5194/egusphere-2026-3109
Preprint. Discussion started: 13 July 2026

employed across the three experiments: class B (moderately unstable), class C (slightly unstable), class D (neutral), and class F (moderately stable). A visualization of plume structure as a function of stability class can be seen in Supplementary Fig. S3. In Experiments 1 and 2, the Pasquill class was held fixed within each scenario; in Experiment 3, the dispersion coefficients were interpolated between endpoint classes as described in Sect. 2.6. For our treatement of non-dimensionalization, coefficients are averaged for the duration of an individual flight profile.

2.2.3 Area-source integration

The circular lake was represented as a superposition of point sources distributed across its surface. The source disk was discretized into $N_r = 20$ concentric radial rings and $N_\phi = 36$ azimuthal sectors, and the concentration enhancement at each receptor was computed by summing the point-source contributions from all source elements:

$$C_i = \sum_{m=1}^{N_r} \sum_{n=1}^{N_\phi} C_{\text{pt}}\left(x_{d,mn}, y_{c,mn}, z_i\right) F_0\, \delta A_{mn} \tag{14}$$

where C_{pt} is the point-source kernel (Eq. (11)) evaluated at the downwind and crosswind distances from source element (m,n) to receptor i, F_0 is the prescribed surface flux, and δA_{mn} is the area of the source element. The emission rate Q in Eq. (11) is replaced by $F_0\, \delta A_{mn}$ for each element. Convergence tests confirmed that the default quadrature of 20 radial rings and 36 azimuths (720 source elements) was sufficient to represent the concentration field to within 1% of a finer reference solution.

2.2.4 Meteorological conditions

All experiments prescribed a spatially uniform, height-invariant horizontal wind field with a reference speed of $U = 2\,\mathrm{m\,s^{-1}}$ and a mean wind-from direction of 225° for visualization (southwesterly). A wind speed of 2 $\mathrm{m\,s^{-1}}$ is representative of the light-wind conditions under which multirotor UAS operations are most practical and during which stable stratification, the regime that most challenges the retrieval, is most commonly encountered (Stull, 2012). The height-invariant wind assumption means that stability effects in the forward model manifest exclusively through the dispersion geometry (Eqs. 12–13), rather than through vertical wind shear. This is a deliberate simplification that isolates the role of plume shape in retrieval performance.

2.3 Sensor representation

Simulated UAS methane mole fraction measurements were generated by applying an instrument noise model representative of the LI-COR LI-7810 trace gas analyzer to the Gaussian plume. The LI-COR LI-7810 is a heavy instrument (10.5 kg) which requires a heavy-lift drone to operate. However, it has high precision and accuracy, useful for determining the upper limit of what is possible with portable gas samplers. The effective measurement precision at a given *dwell time* t_{dwell} (the time spent sampling at each receptor position) was modeled as

https://doi.org/10.5194/egusphere-2026-3109
Preprint. Discussion started: 13 July 2026

$$\sigma_{c,\text{receptor}}(t_{\text{dwell}}) = \max\left(\frac{\sigma_{1\text{s}}}{\sqrt{t_{\text{dwell}}}},\ \sigma_{\text{floor}}\right) \tag{15}$$

where $\sigma_{1\text{s}} = 0.60\,\text{ppb}$ is the 1-second precision and $\sigma_{\text{floor}} = 0.25\,\text{ppb}$ is the minimum precision achievable through extended averaging. The simulated measurement at each receptor is then sampled from random Gaussian noise.

Wind measurement uncertainty was represented at the retrieval stage as Gaussian perturbations to the wind speed and direction supplied by the forward model, with standard deviations of $\sigma_U = 0.3\ \text{m}\,\text{s}^{-1}$ and $\sigma_{\text{wd}} = 10°$, respectively. These values are consistent with the accuracy of lightweight UAS anemometry systems under moderate wind conditions (Thielicke et al., 2021). After perturbation, the wind speed at each height level was averaged across all azimuthal positions at that level. This assumption is consistent with the assumption that there is minimal variation in wind across the x and y dimensions. No GPS position error was applied.

2.4 Experiment 1: Effects from receptor resolution

2.4.1 Motivation

During a real UAS measurement profile, azimuthal resolution along the flight path is governed by the platform's airspeed and the temporal averaging applied in post-processing, while vertical resolution is set by the spacing of flight levels in the ascending or descending profile. These two dimensions of the receptor grid may have asymmetric effects on retrieval performance and trade off differently against total mission duration. This experiment isolated the relationship between the spatial discretization of the cylindrical control surface and the resulting retrieval accuracy and precision under a fixed, steady atmosphere, with all other sources of variability held constant.

2.4.2 Experimental design

The candidate receptor designs comprised the Cartesian product of seven azimuthal sampling counts ($n_{\text{az}} \in \{8, 16, 24, 36, 48, 72, 96\}$), six vertical level counts ($N_z \in \{5, 10, 20, 25, 40, 50\}$), and three Pasquill stability classes (B, D, F), yielding 126 design–class combinations. For a given N_z, vertical receptor levels were placed at the midpoints of equal-height bins spanning the column from the surface to $H_{\text{top}} = 100$ m:

$$z_k = \frac{(2k-1)}{2N_z} H_{\text{top}}, k = 1, \ldots, N_z \tag{16}$$

so that the vertical spacing was $\Delta z = H_{\text{top}}/N_z$. The Gaussian forward plume was generated once for each design–class combination under a fixed wind speed of $2\ \text{m}\,\text{s}^{-1}$ and wind direction of 225°. The resulting truth field was then held constant across 100 replicates, each of which applied an independent realization of sensor noise represented by the first standard deviation before running the cylindrical mass-balance retrieval with height-averaged observed wind.

https://doi.org/10.5194/egusphere-2026-3109
Preprint. Discussion started: 13 July 2026

2.5 Experiment 2: Nearby-lake contamination

2.5.1 Motivation

In heterogeneous wetland–lake landscapes, methane sources other than the target lake may lie in close proximity to the control volume. The cylindrical mass-balance formulation should, in principle, suppress flux from external sources that enters and subsequently exits the cylinder without contributing net divergence. However, because the retrieval resolves only the advective component of the lateral flux (Eq. 4), flux that diffuses across cylinder faces orthogonal to the mean wind may not be fully accounted for, producing a systematic bias. This experiment tested the control volume technique's ability to reject contamination from a nearby upwind lake as a function of inter-lake separation distance and atmospheric stability.

2.5.2 Experimental design

The target lake retained a diameter of 100 m and a prescribed flux of 50 $\mathrm{mg\,CH_4\,m^{-2}\,d^{-1}}$. A secondary lake of diameter 50 m was placed directly upwind of the target at an azimuth of 225° (aligned with the mean wind-from direction), with the same source flux as the target lake. The center-to-center separation between the two lakes was varied from 200 to 1000 m in increments of 100 m. Three Pasquill stability classes were tested (C, D, and F), and the receptor grid comprised 96 azimuthal positions and 27 height levels spanning 0.1–20 m.

For each stability class, a clean baseline retrieval was first generated using the same lake, receptor geometry, and meteorology but with no secondary source present. For each class–distance combination, 100 replicates were then run with contaminated truth fields that included concentration contributions from both the target and nearby lakes. To isolate the contamination effect, the same sensor noise seed was applied to both the contaminated and paired clean retrievals within each replicate. The contamination-induced bias was defined as

$$\mathrm{Bias}_{\mathrm{contam}} = \frac{F_{\mathrm{ret,contam}} - F_{\mathrm{ret,clean}}}{F_0} \times 100\%. \tag{17}$$

Additionally, a lateral exit fraction was computed which partitioned the contamination flux into inward and outward components through the cylinder wall:

$$f_{\mathrm{exit}} = \frac{\sum_{i:\,C_{\mathrm{contam},i}\,v_{r,i}>0} C_{\mathrm{contam},i}\,v_{r,i}\,\Delta A_i}{\left|\,\sum_{i:\,C_{\mathrm{contam},i}\,v_{r,i}<0} C_{\mathrm{contam},i}\,v_{r,i}\,\Delta A_i\,\right|} \times 100\%. \tag{18}$$

A lateral exit fraction of 100% indicates that all contaminant methane entering the control volume through the upwind face also exits through the downwind face, producing zero net contamination of the retrieved target-lake flux. Values below 100% indicate that some portion of the contaminant flux is not recovered by the retrieval.

https://doi.org/10.5194/egusphere-2026-3109
Preprint. Discussion started: 13 July 2026

2.6 Experiment 3: Sampling under evolving atmospheric stability

2.6.1 Motivation

The cylindrical mass-balance retrieval (Eq. 4) treats all measurements on the control surface as 'simultaneous' which is not true for a real mission. For a UAS sequentially visiting thousands of receptor positions over tens of minutes to hours, the atmospheric state, including wind speed, wind direction, and stability, may evolve appreciably during the mission, causing the plume structure observed at early receptor visits to differ from that at later visits. Because the retrieval collapses all observations to a single integral, it cannot distinguish a spatial concentration gradient (which contains flux information) from a temporal change in the plume (which does not). This experiment quantified the resulting non-simultaneity bias as a function of mission duration and the rate of atmospheric change, with wind measurement uncertainty disabled to isolate the temporal effect.

2.6.2 Atmospheric stability transition model

Atmospheric evolution was represented as a smooth, prescribed transition between two Pasquill stability endpoint classes over a 12-hour window, intended to represent the diurnal stabilization of the boundary layer from midday through evening. Pasquill classes were assigned for constructing smooth synthetic transitions; these values are not intended as observational class boundaries. Each Pasquill class was mapped to a Monin–Obukhov stability parameter, ζ (Golder, 1972):

$$\zeta_A = -2.0, \zeta_B = -1.0, \zeta_C = -0.5, \zeta_D = 0.0, \zeta_E = 0.5, \zeta_F = 2.0 \tag{19}$$

and the stability coordinate was linearly interpolated through the transition. The same interpolation was applied to linearly blend the Briggs dispersion coefficients (Eqs. 12–13) between the start and end classes. This stability transition model is heuristic rather than prognostic: it does not solve the surface energy balance or evolve the boundary layer depth, and the nominal stability coordinates (Eq. 19) serve only to create a smooth continuum between discrete Pasquill classes in the dispersion coefficient space. Three stability transitions were considered, representing increasingly strong shifts toward stable stratification: B$\rightarrow$D, C$\rightarrow$D, and C$\rightarrow$F.

2.6.3 Empirical wind variability from AmeriFlux

To represent realistic, stability-dependent variability in wind speed and direction during the simulated missions, we parameterized 30-minute wind statistics as functions of the ζ using eddy-covariance data from the AmeriFlux BASE network (Pastorello et al., 2020). Half-hourly records from multiple sites at all tower heights (~2-40 m) were pooled, retaining only observations that satisfied the following quality criteria: horizontal wind speed $\geq 1\ \mathrm{m\,s^{-1}}$; quality-control flag ≤ 1 when available; finite and nonzero Monin–Obukhov length L; finite lateral and longitudinal velocity standard deviations (U_σ, V_σ); turbulence intensity $TI = U_\sigma/U \leq 10$; and wind-direction standard deviation $\mid \sigma_\theta \mid \leq 90°$, calculated from (Belušić and Mahrt, 2008):

https://doi.org/10.5194/egusphere-2026-3109
Preprint. Discussion started: 13 July 2026

$$\sigma_\theta \approx \frac{V_\sigma}{U}\frac{180^\circ}{\pi}. \tag{20}$$

The retained records were expressed in terms of $\zeta = z/L$, clipped to the range $[-5, 5]$, and binned into 40 equal-width ζ intervals. Within each bin, the median values of U_σ and σ_θ were computed, and piecewise-cubic functions were fit to the bin medians to obtain continuous relationships $\sigma_u(\zeta)$ and $\sigma_\theta(\zeta)$.

At each 30-minute meteorological boundary during a simulated mission, wind speed and direction were drawn from Gaussian distributions centered on the prescribed mean values ($U_{\text{mean}} = 2\ \mathrm{m\,s^{-1}}$, $\text{WD}_{\text{mean}} = 225^\circ$). Wind speed, wind direction, and Briggs dispersion coefficients were then linearly interpolated to the exact sampling time of each receptor visit within the 30-minute interval.

2.6.4 Sequential sampling design

The default receptor grid comprised 96 azimuthal positions and 27 height levels spanning 0.1–20 m above the surface, for a total of $N_{\text{samples}} = 2592$ receptor visits per mission. An adaptive vertical spacing was adopted, with finer resolution concentrated in the lowest meters above the surface to resolve the near-surface concentration gradient that dominates the flux signal under stable conditions. Receptors were visited in a deterministic sequence of increasing height and then increasing azimuth within each height level. The *dwell time* at each receptor was calculated to match a desired mission length divided by the total number of receptors. At each receptor, the interpolated wind speed, wind direction, and blended Briggs dispersion coefficients were evaluated, and the Gaussian plume model generated the instantaneous concentration enhancement at that receptor. Sensor noise was then applied. Mission durations of 30-720 minutes were tested for each of the three stability transitions. Each transition–duration combination was replicated 20 times with independent realizations of the stochastic wind variability to determine precision which is reported as the first standard deviation from the mean.

2.6.5 Repeated-profile strategy

As an alternative to a single extended mission within a changing atmosphere, a series of shorter profiles can be repeated within the same observation window and their independent retrievals averaged. For a sub-flight duration T_{sub}, the 12-hour transition window was partitioned into $N_{\text{rep}} = \lfloor T_{\text{trans}}/T_{\text{sub}} \rfloor$ sequential flights, each traversing the full receptor grid, independently inverted, and the resulting flux estimates averaged. This strategy tests whether temporal averaging of multiple quasi-instantaneous snapshots, each individually noisier but less affected by atmospheric evolution, yields better overall accuracy and precision than a single prolonged integration. The same set of sub-flight durations and stability transitions was evaluated as for the single-flight analysis, allowing direct comparison of the two sampling strategies.

https://doi.org/10.5194/egusphere-2026-3109
Preprint. Discussion started: 13 July 2026

2.7 Nondimensionalizing signal-to-noise and geometry

2.7.1 Motivation

We extend the range of parameterizations found in Experiments 1-3 to evaluate the expected error from different combinations of lake geometry, atmospheric stability, sensor precision, wind speed, and flight duration. We recast the cylindrical-flux retrieval in terms of two nondimensional quantities. The first quantity, Π_S, describes whether the methane measurement at the control surface is large relative to the effective measurement noise. The second quantity, Π_G, describes the size of the lateral extent of the plume relative to the radius of the cylindrical control surface. Together, these variables provide a practical framework to determine the expected error of a proposed lake survey within the Gaussian framework of this paper before conducting a measurement campaign.

2.7.2 Signal-to-noise, Π_S

The signal-to-noise coordinate Π_S is derived from a source-strength leading to a receptor ring-averaged concentration, and an effective retrieval-noise. For a circular lake of radius r_L emitting a spatially uniform lake-mean methane flux F_0 with units of mass per lake area per time, the total methane emission rate is

$$Q_{\text{lake}} = F_0 \pi r_L^2 \tag{21}$$

where Q_{lake} is the total source strength with units of mass per time.

The cylindrical retrieval samples methane concentration on a control surface of radius R_{outer} surrounding the lake. We characterize the signal as the ring-averaged concentration enhancement above background, $\langle \Delta C \rangle$. If the methane is advected outward at mean wind speed U and has a vertical Gaussian dispersion scale $\sigma_z(R_{\text{outer}})$ at the ring, the effective lateral flow area is circumference times cylinder height:

$$A_{\text{eff}} = 2\pi R_{\text{outer}} \sqrt{2\pi}\sigma_z(R_{\text{outer}}) \tag{22}$$

where A_{eff} is the plume-weighted cross-sectional area through which the ring-averaged methane enhancement is transported. The factor $\sqrt{2\pi}$ comes from integrating the Gaussian vertical profile over height (Eq. 23):

$$\int_{-\infty}^{\infty} e^{-z^2/(2\sigma_z^2)} dz = \sqrt{2\pi}\sigma_z \tag{23}$$

Equating the advective methane flux through the effective lateral area to the total lake source gives:

$$Q_{\text{lake}} = \langle \Delta C \rangle U A_{\text{eff}} \tag{24}$$

https://doi.org/10.5194/egusphere-2026-3109
Preprint. Discussion started: 13 July 2026

Solving for the characteristic ring-averaged enhancement,

$$\langle \Delta C \rangle = \frac{Q_{\text{lake}}}{U A_{\text{eff}}} = \frac{F_0 \pi r_L^2}{2\pi\sqrt{2\pi} R_{\text{outer}} U \sigma_z(R_{\text{outer}})} \tag{25}$$

which simplifies to:

$$\langle \Delta C \rangle = \frac{F_0 r_L^2}{2\sqrt{2\pi} R_{\text{outer}} U \sigma_z(R_{\text{outer}})} \tag{26}$$

The effective sensor noise depends on the averaging time assigned to each receptor and the number of receptor locations sampled during the flight. We modify Eq. 15 to account for instruments with different sampling rates. Let $\sigma_{1\text{Hz}}$ be the one-sigma concentration noise at 1 Hz, f_s be the sample rate, and τ_{dwell} be the dwell time at one receptor. The number of samples averaged at one receptor is:

$$N_{\text{samples}} = \tau_{\text{dwell}} f_s \tag{27}$$

the uncertainty in a receptor-mean concentration follows as:

$$\sigma_{c,\text{receptor}} = \frac{\sigma_{1\text{Hz}}}{\sqrt{\tau_{\text{dwell}} f_s}} \tag{28}$$

For $N_{\text{total}} = N_{\text{az}} N_z$ receptor locations, where N_{az} is the number of azimuthal positions and N_z is the number of vertical levels, independent sensor noise reduces the retrieval-level noise on the ring-averaged concentration according to

$$\sigma_{c,\text{retrieval}} = \frac{\sigma_{c,\text{receptor}}}{\sqrt{N_{\text{total}}}} = \frac{\sigma_{1\text{Hz}}}{\sqrt{N_{\text{total}} \tau_{\text{dwell}} f_s}} \tag{29}$$

If the total flight duration is partitioned equally across receptors, then

$$\tau_{\text{flight}} = N_{\text{total}} \tau_{\text{dwell}} \tag{30}$$

and the retrieval-level concentration noise becomes

$$\sigma_{c,\text{retrieval}} = \frac{\sigma_{1\text{Hz}}}{\sqrt{\tau_{\text{flight}} f_s}} \tag{31}$$

Thus, under the white-noise and equal-dwell assumptions, the noise-limited retrieval signal-to-noise ratio depends on the total flight time rather than on how that time is partitioned among receptors.

https://doi.org/10.5194/egusphere-2026-3109
Preprint. Discussion started: 13 July 2026

The resulting dimensionless signal-to-noise ratio Π_S is

$$\Pi_S = \frac{\langle \Delta C \rangle}{\sigma_{c,\mathrm{retrieval}}} \tag{32}$$

390 Substituting the signal and noise scales gives

$$\Pi_S = \frac{F_0 r_L^2 \sqrt{\tau_{\mathrm{flight}} f_s}}{2\sqrt{2\pi} R_{\mathrm{outer}} U \sigma_z(R_{\mathrm{outer}}) \sigma_{1\mathrm{Hz}}} \tag{33}$$

High Π_S indicates that the ring-averaged methane enhancement is large relative to the retrieval measurement noise. Low Π_S indicates that the retrieval is noise limited and that no geometric sampling design can reliably recover the flux without a stronger source, longer integration time, lower wind speed, or more precise sensor.

395 #### 2.7.3 System geometry, Π_G

The second nondimensional variable, Π_G, describes the lateral extent of the methane signal relative to the control-volume radius. For a circular source, the signal width on the receptor ring is controlled by both source-receptor geometry and atmospheric dispersion. A useful envelope scale for the plume width w_{plume} at the receptor ring is:

$$w_{\mathrm{plume}}(R_{\mathrm{outer}}) \approx 2r_L + 2\sigma_y(R_{\mathrm{outer}}) \tag{34}$$

400 where $\sigma_y(R_{\mathrm{outer}})$ is the lateral dispersion scale at the ring. Normalizing by the diameter scale of the control surface gives

$$\Pi_G = \frac{w_{\mathrm{plume}}}{2R_{\mathrm{outer}}} = \frac{r_L + \sigma_y(R_{\mathrm{outer}})}{R_{\mathrm{outer}}} \tag{35}$$

Values of $\Pi_G \approx 1$ indicate that the signal envelope is comparable to the radius of the control surface. Values above one indicate that lateral signal extent is large relative to the ring radius and that mass may be poorly bounded by the sampled cylinder. Values much smaller than one indicate a narrower signal, but not necessarily a uniformly better retrieval, because 405 narrow plumes can be more sensitive to azimuthal sampling and wind-direction variability.

2.7.4 Nondimensional parameter sweep setup

To evaluate the relationship of nondimensional parameters Π_S and Π_G to a variety of different lake and retrieval situations, we sweep across parameters in a changing atmosphere as in Experiment 3. The dimensionless sweep used a receptor design of 96 azimuths and 27 height levels. We varied lake flux F_0 from 5 to 500 $\mathrm{mg\,CH_4\,m^{-2}\,d^{-1}}$, lake radius r_L from 10 to 1000 m, 410 wind speed U from 2 to 5 $\mathrm{m\,s^{-1}}$, and mission duration τ_{flight} from 30 to 90 min. We assign R_{outer} as a ratio to r_L from 1.01 to 3. A Cartesian product of these combination results in 236,250 system configurations. Each configuration used a single flight

https://doi.org/10.5194/egusphere-2026-3109
Preprint. Discussion started: 13 July 2026

beginning at the start of an atmospheric stability transition. We use the same LI-COR LI-7810 trace gas analyzer to define $\sigma_{1\mathrm{Hz}}$ and set $f_s = 1$. Similar to Experiment 3, we include B–D, C–D, and C–F stability transitions. Reverse transitions F–D and D–B are considered in Supplementary Fig. S6.

Calculated Π_S and Π_G from the parameter sweep were then summarized for each atmospheric-transition case within 20×20 bins for each nondimensional variable (Fig. 6). Within each bin, retrieval RMSE for each Π_S and Π_G combination from a set of parameters was calculated between retrieved and prescribed lake-mean flux, F_0. We additionally calculate the standard deviation within each bin, but only for bins containing at least five Π_S and Π_G cases. Thus, each Π_S and Π_G bin represents the aggregate retrieval performance of all dimensional lake, flux, wind-speed, ring-radius, and flight-duration combinations that map to that region of nondimensional space.

3 Results and discussion

3.1 Quadrature error from receptor cell resolution

In our first experiment, we evaluated quadrature error, defined here as the relationship between the spatial resolution of the control-volume receptor grid and the resulting precision and accuracy of the retrieved flux. During a real measurement profile using a UAS platform on a cylindrical control volume, methane mole fraction is typically measured at a fixed instrument cadence, so the operator must decide how to average the resulting data stream through time. Consequently, the spatial-sampling resolution along the UAS flight path is set by the airspeed of the UAS together with any temporal averaging applied in post-processing of the methane data. In contrast, the vertical resolution of UAS orbits on the cylindrical control volume alters the spatial resolution beyond that of airspeed and temporal averaging. We therefore distinguish the number of azimuthal-sampling increments (as defined from the center of the cylindrical control volume), which relates to the time the UAS spends translating along an orbit (e.g., if the UAS is moving slowly, more azimuthal-sampling increments can be defined, while the reverse is true if traveling fast), from the number of vertical levels used to discretize the 100 m cylindrical control volume.

The sensitivity of flux retrievals to receptor-cell resolution is shown in Fig. 2. In general, both accuracy and precision improved with increasing receptor resolution, but the scaling of accuracy and precision differed between azimuthal and vertical refinement. Increasing the number of azimuthal increments primarily increased precision at fixed vertical resolution (e.g., for stability class B at 50 vertical levels on a 100 m cylindrical control volume, $\pm$6.03 $\mathrm{mg\,CH_4\,m^{-2}\,d^{-1}}$ (1σ) at 8 azimuthal cells versus $\pm$3.57 $\mathrm{mg\,CH_4\,m^{-2}\,d^{-1}}$ (1σ) at 96 azimuthal cells). For a given number of vertical levels, the retrieval tended to slightly underestimate the true flux, with a similar bias of -4.37 $\pm$ 0.68% (1σ), -3.08 $\pm$ 1.30%, and -29.17 $\pm$ 1.22% across all azimuthal resolutions tested for stability class B, D, and F respectively. One reason for this has to do with *midpoint-rule* calculations at the lowest vertical level. The Gaussian-plume mole fractions are highest near the surface, and because we define the lowest vertical level as extending from the surface to the midpoint between vertical levels 1 and 2, the *midpoint rule* assigns a single measured value to represent a layer whose true mole fraction increases monotonically toward the ground. Hence, the midpoint value underestimates the mean mole fraction in the lowest vertical level, and since this is the layer that contributes most to the total lateral flux, the retrieval is biased low. Variations in the vertical resolution strongly affected retrieval bias and its dependence

https://doi.org/10.5194/egusphere-2026-3109
Preprint. Discussion started: 13 July 2026

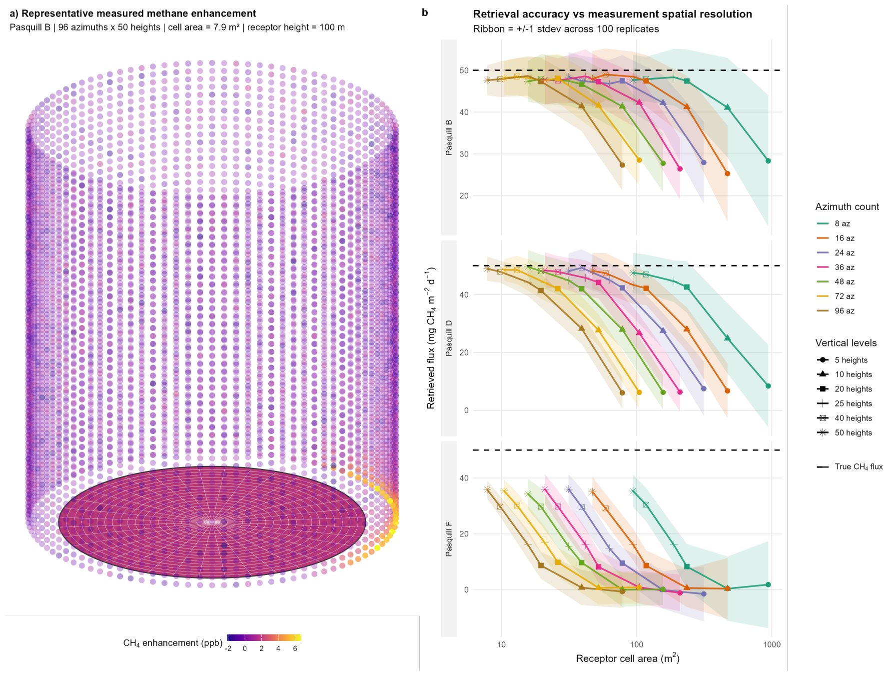

Figure 2. Effect of receptor spatial resolution on whole-lake methane flux retrieval under constant atmospheric conditions. (a) Representative measured methane enhancement for a 100 m diameter lake emitting 50 $\mathrm{mg\,CH_4\,m^{-2}\,d^{-1}}$, shown for the highest-resolution receptor configuration used in the sweep. Points indicate receptor measurements on the cylindrical retrieval surface, with color showing methane enhancement. (b) Retrieved flux as a function of receptor cell area for Pasquill stability classes B, D, and F. Lines show the mean retrieved flux across 100 replicates, ribbons show $\pm$ 1 standard deviation, and the dashed line indicates the true lake flux. Smaller receptor cell areas generally reduce bias, especially under stable conditions where the plume is vertically compressed and more sensitive to receptor spacing.

on stability class: at coarse vertical resolution (10 m spacing), the retrieval underestimated true flux by almost 50% under unstable and near-neutral conditions and by nearly 100% under stable conditions. Under stable conditions, further increasing vertical resolution systematically increased the magnitude of the negative bias (e.g., from -28.30% to -40.55% when decreasing from 50 to 40 vertical levels), whereas in near-neutral conditions comparable changes in vertical resolution produced a smaller change in bias (-2.10% to -4.22%). A visualization of retrieval precision as a function of total receptor-cell count, independent of whether resolution is gained azimuthally or vertically, is provided in Supplementary Fig. S2.

The number of vertical levels on the cylindrical control volume strongly affects quadrature error, which has several implications for UAS flight-plan design. First, since azimuthal-sampling increments are relatively unimportant once a moderate receptor-cell density is achieved, then modifying the UAS velocity is less important than achieving a sufficient number of vertical levels on the cylindrical control volume. Under the stability regimes we explored, the key operational decision becomes the choice of *dwell time* per measurement rather than the number of azimuthal sampling increments. In this paper, *dwell time* was set to ensure that the instrument operated long enough to achieve its precision floor, so the trade-off between increased

https://doi.org/10.5194/egusphere-2026-3109
Preprint. Discussion started: 13 July 2026

dwell time and reduced spatial resolution (azimuthal or vertical) is not explored in this experiment. The strong influence of vertical-level resolution partly depends on the stability-dependent vertical structure of the plume. In stable conditions, the plume remains more confined near the surface, so raising the height of the lowest vertical layer discards a larger fraction of the flux, whereas in neutral and unstable conditions the plume is lofted and near surface flux is less affected by truncation.

These results suggest several practical strategies for mitigating quadrature error, particularly under stable stratification. One option is to increase the radial distance between the lake margin and the cylindrical control volume so that the plume has more space to rise and spread before intersecting with the control-volume surface. This approach would be similar to the optimization of control-volume radius for methane-flux calculations from point sources discussed by Conley et al. (2017). However, in the case of area sources (as in this paper), upwind lake emissions can be transported aloft over longer distances at a given wind speed, increasing the risk that a non-negligible portion of the flux escapes through the top of the cylinder, violating the assumption of zero flux on the top surface of the cylinder (Supplementary Fig. S3). If the atmosphere is known to be stable in the region below the top surface of the cylinder, an operator can safely increase the distance between the lake margin and the cylindrical control volume to reduce quadrature error in the lowest vertical level while still retaining most of the plume within the control volume. A complementary strategy is to employ an adaptive vertical discretization that concentrates vertical levels in the lowest meters above the surface, thereby resolving the near-surface plume while limiting the total number of vertical levels overall (i.e., more vertical levels near the surface and fewer levels higher in the atmosphere). Motivated by these considerations, we adopt an adaptive vertical-discretization scheme in Experiments 2 and 3 to minimize quadrature error.

3.2 Suppressing contamination by nearby sources

In our second experiment, we assessed how effective a cylindrical control volume suppresses contamination from a nearby methane source, such as another nearby lake. In complex, heterogeneous landscapes, enclosing an area source within a control volume isolates that area's flux from nearby emissions. In lake and wetland landscapes, saturated soils and open-water patches that emit methane likely coexist at distances on the order of the length scale of a plume, before the plume's methane concentration becomes indistinguishable from background. In our simulation, we represented contamination as a smaller nearby lake with a similar methane flux of 50 $\mathrm{mg\,CH_4\,m^{-2}\,d^{-1}}$, as the primary larger lake. The smaller lake's methane plume partly intersected the primary lake's control volume on the same axis as the wind direction. The resulting contaminant plume is illustrated in Fig. 3a, and the associated retrieval bias as a function of distance between the lakes centers is shown in Fig. 3b. Across all three atmospheric stability regimes, the contaminant-methane source consistently induced a negative bias in the retrieved flux, with the stable-atmosphere case exhibiting the weakest bias at a lake-center separation of 200 m (-0.40%) and the more neutral- and unstable-atmosphere cases showing larger negative biases (-3.81% and -7.52%, respectively).

The systematic negative bias induced by the contaminant-methane source from the smaller lake arises from the assumption of purely advective transport in the *cylindrical-flux method*. By neglecting the turbulent diffusive term in the divergence of the flux, the method underestimates any component of contaminant flux that diffuses across the control volume boundary orthogonal to the advective flow. Conceptually, consider the schematic in Fig. 4: a contaminant plume enters an octagonal control volume under a uniform horizontal wind field. The retrieved flux is the dot product of the local concentration and wind

https://doi.org/10.5194/egusphere-2026-3109
Preprint. Discussion started: 13 July 2026

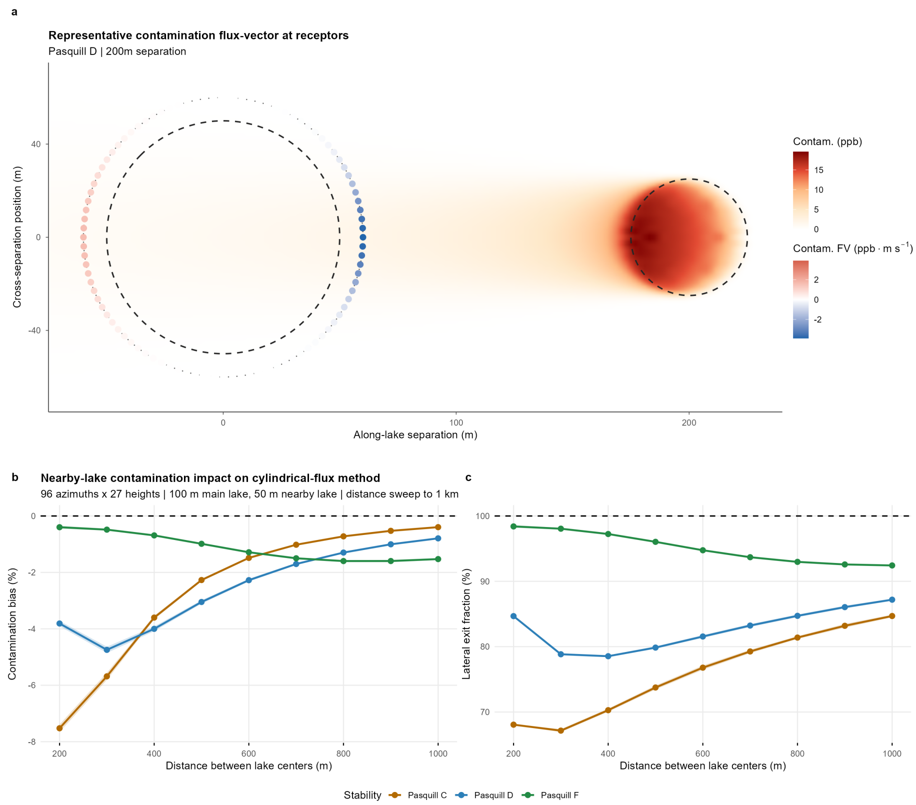

Figure 3. Nearby-lake contamination effects on methane flux retrievals by lake separation distances. (a) Representative top-down plume view at z = 0.1 m for a 50 m diameter nearby lake located 200 m from the center of a 100 m diameter target lake under Pasquill D stability. The raster shows nearby-lake CH_4 contamination at the lowest receptor height, dashed circles mark the lake boundaries, and the dotted circle marks the cylindrical measurement receptor cells. Receptor colors show the nearby-lake contamination flux-vector contribution, where positive and negative values indicate outward and inward contributions through the control surface. (b, c) Mean contamination bias and lateral exit fraction as a function of lake-center separation from 200 to 1000 m for Pasquill C, D, and F stability. Lines show means and ribbons show $\pm$ 1 standard deviation across 100 repetitions. Both lakes emit 50 $\mathrm{mg\,CH_4\,m^{-2}\,d^{-1}}$.

vector with the outward normal at each receptor cell, so cells whose normals are perpendicular to the wind contribute zero flux for the portion of the plume that has diffused into them. Similarly, plume flux that enters through the upwind face and later diffuses into faces that are oblique to the mean wind vector is reduced in proportion to the cosine of the angle between the local normal and the advective direction. The most strongly diffused components of the plume therefore contribute the smallest fraction of the total accounted flux, and the net lateral-exit fraction (Eq. 18) recovered by the *cylindrical-flux method* becomes a function of plume geometry, wind speed, and stability class.

The simulated plume geometry is characterized by the Gaussian parameters in Eq. 11, including the mean wind speed, wind direction, and the dispersion parameters σ_y and σ_z (which control lateral and vertical diffusion). These σ values increase more

https://doi.org/10.5194/egusphere-2026-3109
Preprint. Discussion started: 13 July 2026

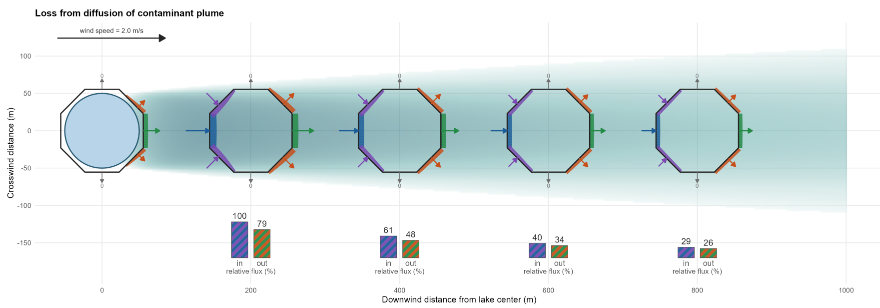

Figure 4. Conceptual top-down schematic of plume loss from diffusion through control-volume faces. A 100 m diameter lake is represented as an area methane source in stability class F atmosphere, producing a downstream analytical Gaussian plume under steady 2 $\mathrm{m\,s^{-1}}$ wind. Identical octagonal Conley control volumes are translated along the plume centerline. Colored face bands and arrows show the integrated face-normal plume flux through each control volume face, with arrow length and face band scaled by flux magnitude. Blue and purple indicate plume entering through the direct upwind and oblique upwind faces, respectively; green indicates plume leaving through the opposite downwind face; orange indicates plume leaving through lateral/oblique faces. Gray arrows mark faces with zero normal flux on account of being perpendicular to the wind field. Bar plots beneath each control volumes summarize total initial plume input and output as relative flux, illustrating that as atmospheric diffusion broadens the plume, an increasing lateral fraction (out/in) exits through non-opposing faces and is therefore represented as control-volume loss rather than direct downwind transfer.

rapidly in unstable conditions than in neutral or stable conditions, leading to broader plumes and stronger diffusion at a given downwind distance. Wind speed modulates how much diffusion is able to occur within the control volume. Higher wind speeds cause faster advection of the plume, limiting the time for diffusion within the control volume. Lower wind speeds, in contrast, allow for greater diffusion within the boundaries of the receptor cells, in which case the plume can spread to more oblique receptor cells, incurring a more significant flux retrieval underestimation. Further, wind direction determines whether and where the contaminant plume intersects with the control cylinder. In our simulations, wind direction was aligned to maximize intersection with the control volume. In contrast, a wind direction that causes the plume to partially intersect with the control volume would have a fractional effect. Taken together, the net effect of contamination is governed by the amount of the plume that both enters the control volume and then diffuses away from the strictly advective path while still inside it.

When we varied the separation between the primary lake and the contaminant lake in unstable and neutral atmospheres, flux retrieval accuracy improved with increasing distance between the lakes. Contamination-induced bias decreased from -7.52% at 200 m lake-center separation to -0.40% at 1 km separation as the plume approached the background signal in an unstable atmosphere. In stable conditions, the contamination induced bias was initially small at 200 m lake-center separations, because σ_y and σ_z were small and the contaminant plume remained narrow. The bias increased at intermediate distances which allowed diffusion of the plume within the control volume to reach a maximum, however if lake separation continued to increase, the bias reduces, trending towards the plume becoming indistinguishable from background at large distances. Lake area also modulated the contaminant effect. We chose the contaminant lake to be smaller than the primary lake, which resulted in relatively large diffusion gradients at the primary lake's control-volume boundary and thus the potential for diffusive loss. As the contaminant

https://doi.org/10.5194/egusphere-2026-3109
Preprint. Discussion started: 13 July 2026

lake gets larger, the upwind source increasingly resembles a spatially uniform background field as it passes through the control volume. For an upwind-contaminant source area that is infinitely large, the diffusion gradient vanishes entirely. Besides this, an additional means of producing greater contamination is a greater methane flux at the contaminant source. Since the Gaussian plume forward model scales linearly with flux, the contamination bias scales linearly as well for the same lateral-exit fraction which is only determined by plume geometry.

These contamination effects have important implications for UAS sampling campaigns in heterogeneous environments that produce methane emissions. The contamination bias is maximized for small-area contaminant methane sources (or point sources) at intermediate distances from the control volume, and the bias is minimized for large or distant sources whose plumes effectively converge on the background signal. In our simulations, contaminant plumes within unstable and near-neutral atmospheres became indistinguishable from background (<1% bias) at distances of >2 km upwind of the primary lake's control volume (Supplementary Fig. S4), consistent with the expectation that unstable and near-neutral atmospheres are relatively well mixed at multi-kilometer scales (Stull, 2012). With stable atmospheres, influential contaminant sources can occur at lake-separation distances where the signal would have already diffused to background in unstable and neutral atmospheres. In practice, the most robust mitigation of the contamination effect is to perform measurements so that known contaminant sources lie downwind of the primary lake, ensuring that their plumes do not intersect the control volume.

3.3 Flying longer reduces accuracy in a changing atmosphere

Up to this point, we have assumed constant atmospheric stability, wind speed, and wind direction, and varied only the receptor and source geometry to diagnose flux-retrieval uncertainty. In our third experiment, we relax the assumption of constant atmosphere and impose a transient atmosphere. In reality, the atmosphere evolves continuously, so choices about how long to sample and how many receptors to occupy will be a trade off with errors introduced by a changing plume. Atmospheric variability can span many time scales, for example, large turbulent eddies can modulate wind speed and direction from second-to-minute scales (which perturb the wind inputs to the *cylindrical-flux method)*, while diurnal changes in surface heating and synoptic forcing can drive transitions between stability regimes over hours (Stull, 2012). An intuitive response to second-to-second atmospheric variability is to increase *dwell time* at each receptor but this comes at the cost of sampling over a longer time interval during which the background state and plume structure may evolve appreciably.

We examined flux retrievals under prescribed transitions between three archetypal stability-class pairs that occur across a 12-hour period (Fig. 5b). Across all three stability transitions, moderately unstable-neutral (B–D), slightly unstable-neutral (C–D), and slightly unstable-moderately stable (C–F), the highest flux-retrieval accuracy was obtained with the shortest flight (30 min). Note that for any flight duration (i.e., 30 min, 1 h, etc.), the flight starts at the beginning of the 12-hour period. Compared to the true lake flux of $50\ \mathrm{mg\,CH_4\,m^{-2}\,d^{-1}}$, 30 min flights resulted in retrieved fluxes of $47.85 \pm 0.89\ \mathrm{mg\,CH_4\,m^{-2}\,d^{-1}}$, $49.19 \pm 0.97\ \mathrm{mg\,CH_4\,m^{-2}\,d^{-1}}$, and $49.17 \pm 1.12\ \mathrm{mg\,CH_4\,m^{-2}\,d^{-1}}$ (1σ) for atmospheric stability transitions B–D, C–D, and C–F, respectively. As flight duration increased and more time was spent at each receptor, accuracy systematically degraded because the plume shifted with the changing atmospheric stability. Starting with an unstable atmosphere and transitioning towards a neutral or stable atmosphere shifts the plume downwards over the 12-hour period. Since the UAS samples the lowest

https://doi.org/10.5194/egusphere-2026-3109
Preprint. Discussion started: 13 July 2026

height levels first (when the plume is unstable and well-mixed), by the time the UAS reaches the upper levels of the profile, the atmosphere has transitioned toward a more stable atmosphere, and the plume has contracted toward the surface (Fig. 5a). In this case, the UAS measured well-mixed methane on the lower portions of the control volume but then measured lower methane at the top of the control volume than would have been measured at the beginning of the flight. When the shape and vertical extent of a plume is changing in time, the *cylindrical-flux method* cannot distinguish the transitory nature of the plume, instead implicitly assuming it represents a snapshot. This results in a temporal bias in the methane-flux retrieval (lower flux than truth), because the plume was contracting while the UAS was ascending. In the converse case, where the atmosphere starts stable and becomes unstable (such as stability transitions F–D or D–B; Supplementary Fig. S5), a rising plume with an ascending UAS results in an overestimation in the retrieval flux. The loss in accuracy (-12.30% for B–D, -5.65% for C–D, and -13.74% for C–F) scaled with the magnitude of the change in ζ of the underlying stability transition. Flux retrieval precision improved with total flight time but exhibited diminishing returns; for example, in the C–D transition, extending measurement time from 30 min to 2.5 h reduced the flux retrieval standard deviation over 20 repetitions of the profile from ±0.97 $\mathrm{mg\,CH_4\,m^{-2}\,d^{-1}}$ to ±0.43 $\mathrm{mg\,CH_4\,m^{-2}\,d^{-1}}$, whereas a further extension to 12 h yielded only a marginal gain to ±0.23 $\mathrm{mg\,CH_4\,m^{-2}\,d^{-1}}$. The marginal gain results from increasing the measurement time at each receptor cell. A 30 min flight resolving 96 azimuth increments and 27 vertical levels corresponds to sampling near the 1 Hz measuring rate of the instrument, while a 12 h flight implies roughly 17 s of averaging per receptor, which easily achieves the assumed methane precision floor of the instrument. Within the range of stability transitions tested over 12 h, flying as fast as possible preserved the highest accuracy. The modest reduction in flux retrieval precision of short flights relative to longer flights was smaller than the magnitude of accuracy loss from flying longer in a changing atmosphere.

Under changing atmospheric stability, one might choose to repeat short flights multiple times to approximate an average plume over a certain time period. We evaluated this strategy by repeating profiles of varying duration within the same 12 h window, for example, flying a 30 min profile 24 times in the 12-hour period or a 1 h profile 12 times in the 12-hour period. Since shorter flights permit more repetitions, individual short flights have lower precision of flux retrieval than intermediate-length flights (as discussed in the prior paragraph). When we repeated profiles across B–D, C–D, and C–F stability transitions, flux retrieval precision was broadly similar across flight durations between 30 min and 2 h and was substantially improved relative to a single flight that began at the start of the 12-hour period. Across 20 repetitions of the multi-profile flights, the average standard deviation of flux retrieval improved to ±0.30 $\mathrm{mg\,CH_4\,m^{-2}\,d^{-1}}$ for 30 min to 2 h flights. Accuracy also improved slightly compared with single 30 min flights, with mean bias reduced by 2.21%, 2.21%, and 0.61% for the B–D, C–D, and C–F transitions, respectively. The dependence of bias on flight duration within the repeated-profile strategy mirrored the single-flight behavior: C–D exhibited the smallest increase in bias with longer individual flights from 30-90 min (0.61% versus 0.17%), followed by B–D (0.68% versus 0.36%) and C–F (2.21% versus 1.62%). Across all single and multi-profile flight simulations, the best-performing approach was to fly 30 min profiles, corresponding to approximately ~1 s averages per receptor cell and a ground speed of ~20 $\mathrm{km\,h^{-1}}$, and to repeat 30 min profiles as much as possible during the 12-hour period rather than extending single flights to multi-hour duration. However, the marginal gain in accuracy of multiple 30 min flights

https://doi.org/10.5194/egusphere-2026-3109
Preprint. Discussion started: 13 July 2026

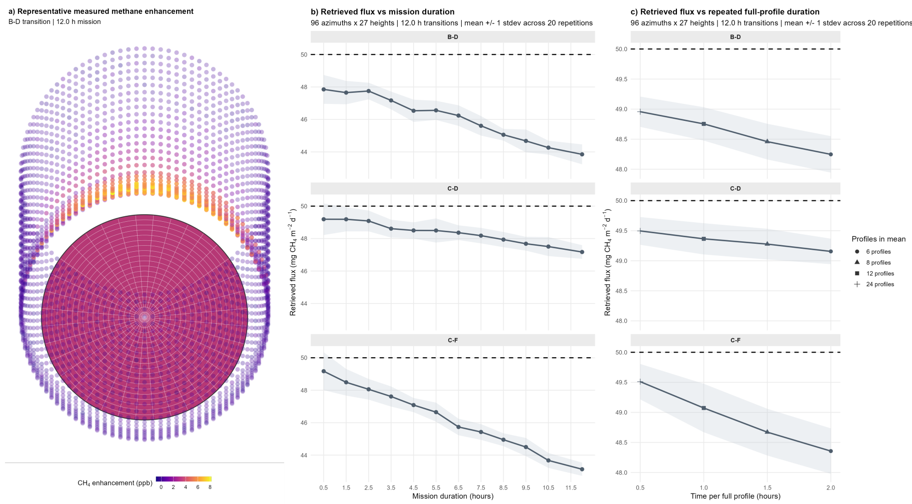

Figure 5. Flux retrieval sensitivity to sequential sampling during a changing atmosphere. (a) Representative measured $\mathrm{CH_4}$ enhancement field for a 12 h B–D stability transition for a 12 h mission. Points show sequential receptor measurements from the cylindrical sampling surface. (b) Retrieved flux from single sequential missions of increasing duration which start at the beginning of the measurement period (c) Retrieved flux when repeated full-profile measurements are made over the 12 h transition window and are averaged; point shape indicates the number of full profiles included in the mean. Panels in b and c show primary transitions B–D, C–D, and C–F. Lines are means, ribbons are $\pm$ 1 standard deviation across 20 repetitions, and the dashed horizontal line marks the true flux of 50 $\mathrm{mg\,CH_4\,m^{-2}\,d^{-1}}$.

585 (a change in bias of 0.68%) relative to performing a single 30 min flight may not be worth the extra time in real world field campaigns.

3.4 Retrieval-error regimes in nondimensional space

Nondimensional analysis was designed as a practical approach to build an expectation of *cylindrical-flux method* accuracy under different source, environmental and system configurations. For a proposed lake and UAS payload under different atmo-
590 spheric conditions, a user can estimate F_0, r_L, R, U, τ_{flight}, f_s, and $\sigma_{1\mathrm{Hz}}$, choose representative atmospheric change, compute Π_S and Π_G, and then locate the case in the retrieval error bins (Fig. 6a). The bins should be interpreted as expected error regimes rather than deterministic predictions of retrieval accuracy, because the bins contain physically different scenarios which results in a common nondimensional value but with some variability on the resulting retrieval accuracy (Fig. 6b).

The signal-to-noise nondimensional parameter Π_S showed significantly increased accuracy performance systematically as
595 it increased (Table 1). Cases with $\Pi_S < 1$ had a median absolute error of approximately 106% and only 12% of scenarios were retrieved within 25% of the true flux. For $\Pi_S \geq 50$, the median absolute error decreased to approximately 10%, and approximately 70% of scenarios were retrieved within 25% of the prescribed flux. This monotonic improvement supports interpreting Π_S as the primary indicator of the connection between measurement uncertainty and methane flux available to measure.

https://doi.org/10.5194/egusphere-2026-3109
Preprint. Discussion started: 13 July 2026

Table 1. Retrieval performance grouped by Π_S across the full wind-speed sweep. RMSE is reported relative to the prescribed lake-mean methane flux.

Π_S	RMSE (%)	Median absolute error (%)	Within 25% RMSE (%)
$\Pi_S < 1$	690	106	12
$1 \leq \Pi_S < 5$	286	48	30
$5 \leq \Pi_S < 10$	167	27	47
$10 \leq \Pi_S < 50$	93	14	66
$\Pi_S \geq 50$	45	10	70

However, the $\Pi_S \geq 50$ region still retained a substantial high-error tail, indicating that signal detectability by measurement is necessary but not sufficient for accurate retrieval.

The geometric nondimensional variable Π_G represents the width of the plume at the receptor cell boundary relative to the receptor distance from the lake center. This geometric relationship probes the extent of diffusive loss downwind like shown for a contaminant lake in Experiment 2. The Π_G value for a system also interacts non-linearly with quadrature error as the plume moves through an evolving atmosphere as in Experiment 3. The resulting relationship to retrieval accuracy was less interpretable than Π_S. After filtering for sufficient signal-to-noise ($\Pi_S > 10$), no Π_G boundary separated accurate and inaccurate retrievals in a simple way. This does not invalidate Π_G as a nondimensional coordinate. Rather, it reinforces that lateral spread interacts with signal strength, wind-direction variability, stability-transition pathway, and source geometry. For a given Π_G, the relationship for retrieval accuracy versus Π_S can be defined. Thus, Π_G is most useful as a coordinate for deconvoluting the system geometry between lake area and receptors to select an appropriate Π_S, but cannot be used as a cutoff for *cylindrical-flux method* accuracy performance.

The atmosphere stability transition had varying importance after nondimensionalization. In the transitions, stability classes B–D, C–D, and C–F (Fig. 6) had similar retrieval RMSE in Π_S–Π_G space. The F–D case presented in Supplementary Fig. S6, showed substantially larger negative bias and higher error even within the higher Π_S region, with RMSE of approximately 112% and only 53% of scenarios within 25% of the true methane flux. Outside of the F–D case, similar performance across the other atmospheric stability shifts indicates that the same nondimensional variables can be predictive of *cylindrical-flux method* accuracy regardless of how atmospheric stability evolves during the flight.

The Π_S and Π_G statistics reported within bins are useful for communicating feasibility, but they should be interpreted probabilistically. Across all 236,250 combinations of parameters we explored in the nondimensional parameter sweep, 61.9% of retrievals were within 25% of the true flux. Restricting to the nominal favorable region with $\Pi_S > 10$ and $\Pi_G < 1$ increased this fraction to 69.7% and reduced the median absolute error from 15.1% to 9.6%. The improvement demonstrates that the nondimensional variables provide useful survey-design information, but do not define a strict accuracy guarantee. The variability in RMSE across different Π_S and Π_G is higher than the effects presented in Experiments 1, 2 and 3 because changing nondimensional variables explores varying a higher number of experimental setups but does not directly explore the causes of the underlying error on *cylindrical-flux method* accuracy.

https://doi.org/10.5194/egusphere-2026-3109
Preprint. Discussion started: 13 July 2026

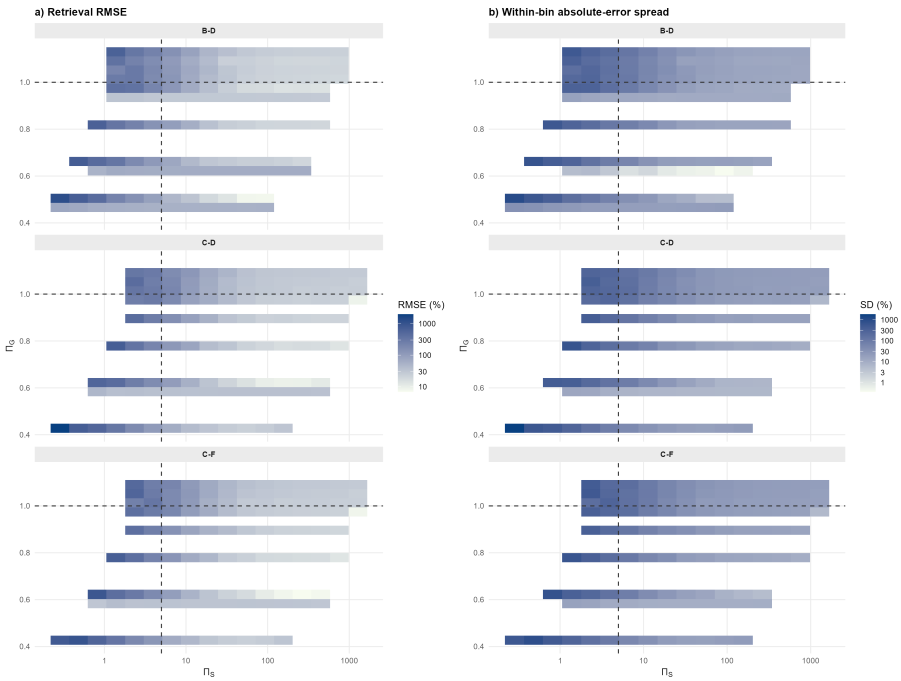

Figure 6. Dimensionless retrieval-error framework for the atmosphere stability transition cases. Rows show B–D, C–D, and C–F atmospheric stability transitions. The left column (a) shows flux-retrieval RMSE, expressed as percent error relative to the prescribed lake-mean flux, binned in 20 bines each for Π_S and Π_G. The right column shows the within-bin spread in standard deviation of bins for bins with at least five values. The vertical dashed line marks $\Pi_S = 5$, a practical low-detectability reference, and the horizontal dashed line marks $\Pi_G = 1$, the theoretical transition where lateral signal extent is comparable to the control-volume radius. RMSE is presented in logarithmic scale and standard deviation in linear scale.

As a working example for evaluating estimate error for a system configuration, consider a 200 m radius lake emitting $F_0 = 25$ $\mathrm{mg\,CH_4\,m^{-2}\,d^{-1}}$, sampled on a 220 m radius ring during a 60 min flight with a 1 Hz sensor precision of 0.6 ppb and a 4 $\mathrm{m\,s^{-1}}$ wind. Using neutral Briggs dispersion gives $\sigma_y(220\text{ m}) = 17.4$ m and $\sigma_z(220\text{ m}) = 11.4$ m at the receptor ring edge. These values yield $\Pi_S \approx 33.2$ and $\Pi_G \approx 0.99$. This case falls in a moderate-to-high signal-to-noise regime. In the bins of the current sweep, the primary B–D, C–D, and C–F transitions at this coordinate had RMSE values of approximately 24%, 43%, and 41%, respectively. The F–D transition at the same coordinate was much less favorable, with RMSE of approximately 189% and median absolute error of approximately 37%. The system's Π_G defines the relationship between accuracy and increasing signal-to-noise as shown in Fig. 7. Should an analogous system produce $F_0 = 75$ $\mathrm{mg\,CH_4\,m^{-2}\,d^{-1}}$, the resulting accuracy follows to be approximately 17%, 25%, and 26% in a B–D, C–D, and C–F transitions, respectively. This example illustrates how the nondimensional framework can be used as a screening tool: a proposed survey can be mapped into Π_S–Π_G space, but the atmospheric-transition context remains necessary for interpreting the expected RMSE.

https://doi.org/10.5194/egusphere-2026-3109
Preprint. Discussion started: 13 July 2026

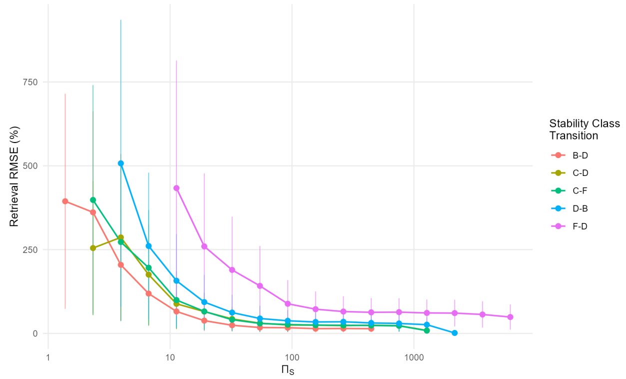

Figure 7. Retrieval RMSE as a function of the signal-to-noise nondimensional group, Π_S, for scenarios falling within the Π_G bin containing the worked-example value (Π_G = 0.99; selected bin range 0.955-0.994). Points show binned RMSE (%) relative to prescribed lake-mean flux, $F_0 = 25\ \mathrm{mg\,CH_4\,m^{-2}\,d^{-1}}$, for differing atmosphere stability transitions. Error bars show the within-bin standard deviation of retrieval error.

3.5 Limitations of the OSSE and additional measurement considerations

There are several limitations of the forward-model and flux retrieval calculations. First, representing atmospheric transport with a Gaussian plume is a significant simplification of the boundary-layer fluid dynamics that actually affect methane transport over a lake. The Gaussian formulation yields a smooth, time-averaged concentration field that does not capture the intermittent, filamentary-structure characteristic of real plumes (Gifford Jr, 1959; Mylne and Mason, 1991). Real plumes meander on time scales much faster than the 30 min observational windows we considered in our simulations from AmeriFlux observations. Additionally, individual sites exhibit wind variability tied to local topography and surface-energy balance that may alter the optimal sampling strategy (Mylne and Mason, 1991; Mahrt, 1999; Warhaft, 2000).

Second, we adopted a horizontally and vertically uniform wind field rather than a wind profile that varies with height. Instead, a wind field that follows the Monin–Obukhov similarity theory (MOST) with height would be more physically realistic. A MOST wind-profile would reduce the signal-to-noise ratio of airborne wind measurements near the surface, where wind speeds are lowest (Monin and Obukhov, 1954; Stull, 2012). Lower wind signal-to-noise is most consequential near the surface under stable stratification, where plume concentrations are greatest and retrieval accuracy is most sensitive to wind uncertainty. One practical mitigation is simply to fly more profiles (as in Experiment 3), capturing more “snapshots” of the atmosphere across the relevant range of wind variations and other conditions. A more rigorous alternative to the simulation of methane flux as a Gaussian plume would be the use of a large-eddy simulation (LES) as the forward model, which would more faithfully represent turbulent transport, plume intermittency, and wind shear (Ražnjević et al., 2022). However, the computational cost of LES precludes a wide exploration of atmospheric conditions and flight configurations that were used in the OSSE approach in this paper.

https://doi.org/10.5194/egusphere-2026-3109
Preprint. Discussion started: 13 July 2026

Third, a further simplification in this OSSE is the assumption of spatially uniform and temporally constant lake emissions. Real-lake methane fluxes are heterogeneous across multiple dimensions: a) spatially, between littoral and pelagic zones (Kyzivat et al., 2022; Tanentzap et al., 2026), b) temporally, through daily cycles driven by surface temperature and gas transfer velocity (Sieczko et al., 2020), and c) episodically through ebullition (bubbling) events (Bastviken et al., 2004; Praetzel et al., 2021). In many methane-productive lakes, ebullition (bubbling) dominates the total methane budget (Wik et al., 2016). Individual bubble-release events are common and generate transient, intense, and near-point-source releases, similar to the transitory problem of a changing plume under varying atmospheric stability that we examined in Experiment 3. In our simulations, a strong ebullition event occurring during one segment of a flight could be aliased as a spatial anomaly in the retrieved flux field rather than as a discrete pulse. More simply, the *cylindrical-flux method* can only measure the total flux passing through its sampling boundary, it cannot resolve how emissions vary within that volume. In the worst-case scenario, the plume associated with an ebullition event might occur during a flight but after the UAS has ascended beyond the plume associated with the ebullition, which would contribute unquantified sampling bias to the retrieved flux. Further, in real turbulent atmospheric flows, the geometry of the methane source – even within the control volume – contributes to how those emissions are transported (Pasquill and Smith, 1983), and our OSSE framework cannot capture that transport.

The OSSE framework presented in this paper was predicated on a hypothetical UAS observing platform. The methane analyzer (LI-COR LI-7810) used as the basis for our simulated sensor has a mass of approximately 10.5 kg, which exceeds the lift capacity of many types of UAS. Lighter methane instruments than the LI-7810 have been deployed on UAS but typically offer lower precision and are challenged by signal-to-noise constraints arising from atmospheric transport uncertainty our Gaussian plume forward model does not evaluate (Shah et al., 2019; Martinez et al., 2020; Shaw et al., 2021). Wind measurement also presents difficulty. Rotor wash from multirotor-UAS platforms introduces systematic errors in the measurement of wind speed and direction, though these can be partially addressed through numerical correction schemes (Jin et al., 2024) or through careful sensor placement away from the rotor-influence zone (Thielicke et al., 2021). As a final consideration, while the flight speeds considered in our simulations are operationally feasible, deploying an expensive instrumented aircraft at low altitude and high speed over topographically complex terrain introduces nontrivial safety and operational risk.

Despite these limitations, the plume geometry over lakes, particularly under stable stratification, creates opportunities for complementary measurement schemes. The weak sensitivity of methane-flux-retrieval precision to azimuthal resolution suggests that a small number of fixed towers (such as eight in total) instrumented with methane analyzers at multiple heights could capture a substantial fraction of the relevant flux signal across a wide range of wind directions. Or, instead of towers, deployment of multiple UAS platforms at the same time could increase the density of concurrent measurements on a control volume, reducing error relative to the use of a single UAS. Multi-platform approaches, including towers or additional UAS, would introduce additional calibration uncertainty across instruments, but offer a path to reducing errors attributable to transient emissions and rapidly evolving atmospheric transport.

https://doi.org/10.5194/egusphere-2026-3109
Preprint. Discussion started: 13 July 2026

4 Conclusions

The heterogeneity of methane emissions from natural systems such as lakes and wetlands has contributed to these systems remaining poorly constrained in global atmospheric inversions and bottom-up inventories of natural-methane sources. A central obstacle is the absence of measurement approaches capable of resolving the spatial variability of methane flux at the scale of individual landscape features (e.g., lakes and wetlands) in complex natural settings.

To quantify methane flux from point-source emissions, Conley et al. (2017) presented an airborne flux-measurement method based on the flux divergence through a cylindrical-control surface. The ability of a closed control volume to isolate a source from contributions outside its boundary, as described by Conley et al. (2017), makes the method a compelling approach to quantify methane flux from heterogeneous natural systems (i.e., systems that are not just a single point source, but rather many sources or an area source). In this paper, we explored whether the Conley et al. (2017) approach was possible using an uncrewed aerial system (UAS) over an area source of methane such as a lake, as well as how contamination from a nearby source of methane, such as a smaller lake, could bias results.

We evaluated area-source emissions through an Observing System Simulation Experiment (OSSE) in which we applied a *cylindrical-flux method* to an idealized methane-producing lake under a range of atmospheric conditions. Three experiments addressed distinct sources of retrieval uncertainty: (1) the effect of receptor-grid resolution on quadrature error arising from the discrete approximation of a continuous concentration field around the lake; (2) the resilience of the retrieval to contamination from a nearby external methane source; and (3) the impact of changing atmospheric variability on retrievals over the course of a 12-hour sampling day. Across all three experiments, we derived recommendations for operators implementing the *cylindrical-flux method* for lake-scale or wetland methane flux estimation.

From Experiment 1, we found that receptor resolution (the size of a single unit of discretized surface from which flux is calculated) plays a modest role in retrieval precision but a significant role in accuracy, because vertical resolution determines how well the control volume captures plumes that are confined near the surface, especially for a stable atmosphere. Experiment 2 demonstrated that the retrieval method can partially suppress contributions from nearby source contamination, but that a residual negative bias persists because the *cylindrical-flux method* formulation accounts for advective transport only and cannot recover flux lost through turbulent diffusion across the control-volume boundary. This bias diminished with increasing separation of the contamination source from the primary lake, with the contaminating plume converging toward a background signal and dropping out of the divergence integral. Experiment 3 showed that retrievals under a changing atmosphere are most accurate when flight duration is minimized, as shorter flights better approximate the quasi-steady-state assumption underlying the method. Instead of a single flight, repeating flight profiles many times improved both accuracy and precision, but the marginal gain did not strongly justify the additional flight time.

The idealized assumptions underlying our experiments limit how broadly the results can be generalized. We introduce nondimensional variables which target both methane measurement signal-to-noise and the lake-receptor geometry. The resulting relationships allow for the determination of *cylindrical-flux method* uncertainties discussed in Experiments 1-3 in a broad span of system configurations. Even with the nondimensional treatment, real lakes exhibit transient, episodic, and spatially

https://doi.org/10.5194/egusphere-2026-3109
Preprint. Discussion started: 13 July 2026

heterogeneous emissions, including ebullition, whose covariance with atmospheric transport cannot be evaluated within our constant-flux framework. The Gaussian plume model we use captures the mean behavior of dispersion but does not represent the intermittent filamentary structure of real boundary-layer plumes, and our prescribed meteorological scenarios do not fully resolve the site-specific variability in wind and stability driven by local topography and radiative forcing. Furthermore, while we modeled sensor and platform characteristics at the limits of current technology, the specific combination of a high-precision methane analyzer, wind measurement system, and UAS airframe required to execute a sampling mission will vary with specific applications and scientific goals, and as technology progresses, the simulations in this paper should be repeated to ensure the best scientific outcomes. It is better to simulate potential outcomes and adjust the sampling strategy before a field deployment, rather than trying to adjust in real time during that field deployment.

Significant gaps remain in our understanding of how real-world emission heterogeneity and turbulent transport affect flux retrieval fidelity under more complex conditions. In future research, the OSSE presented in this paper could be improved in three ways. First, it could employ an Large eddy simulation-based forward model to represent realistic turbulent transport and plume intermittency. Second, the emission field could be partially constrained by lake-scale methane fluxes measured by eddy covariance, anchoring the source term in observations rather than prescribed constants. Third, it could explicitly model an existing UAS platform and sensor suite (rather than the hypothetical platform and sensors we put forward in this paper). In this way, the existing platform and sensors can be tested under the OSSE approach to ensure that the field-measurement campaign will be successful, including considerations of quantifying the practical trade-offs among flight speed, payload mass, measurement precision, and total measurement platform cost. Once the UAS platform and sensor are validated by the OSSE, then a much higher confidence in the results of the field campaign will help to ensure successful scientific outcomes.

Code and data availability. Code and simulation data for this study are available on Zenodo (DOI:10.5281/zenodo.20448713)

Author contributions. KSR: Conceptualization, Methodology, Visualization, Investigation, Formal analysis, Writing – original draft & review & editing, Data curation. EAM: Conceptualization, Methodology, Investigation, Writing – review & editing. IO: Conceptualization, Methodology, Investigation, Writing – review & editing, Supervision. GBR: Funding acquisition, Writing – review & editing, Project administration, Supervision. TRJ: Validation, Funding acquisition, Writing – review & editing, Project administration, Supervision, Data curation, Resources, Conceptualization.

Competing interests. The authors declare no competing interests.

Acknowledgements. This work was supported by U.S. National Science Foundation (NSF) grants 2022561 and 2432536 for the project “Collaborative Research: NNA Track 1: Global impacts and social implications of changing thermokarst lake environments near Yukon River

https://doi.org/10.5194/egusphere-2026-3109
Preprint. Discussion started: 13 July 2026

Watershed communities." Artificial Intelligence (Codex Version 5.5) was used to aid in scripting, figure development, and proofreading prior to submission.

References

Allen, D. T., Chen, Q., Ravikumar, A. P., and Tullos, E. E.: Multiscale Measurement and Modeling of Methane Emissions in US Oil and Gas Production Regions, Annual Review of Chemical and Biomolecular Engineering, 17, 2025.

Arnold, W., Taylor, M., Bradford, M., Raymond, P., and Peccia, J.: Microbial activity contributes to spatial heterogeneity of wetland methane fluxes, Microbiology Spectrum, 11, e02 714–23, 2023.

Aubinet, M., Vesala, T., and Papale, D.: Eddy covariance: a practical guide to measurement and data analysis, Springer Science & Business Media, 2012.

Barker, P. A., Allen, G., Pitt, J. R., Bauguitte, S. J.-B., Pasternak, D., Cliff, S., France, J. L., Fisher, R. E., Lee, J. D., Bower, K. N., and Nisbet, E. G.: Airborne quantification of net methane and carbon dioxide fluxes from European Arctic wetlands in Summer 2019, Philosophical Transactions of the Royal Society A, 380, 20210 192, https://doi.org/10.1098/rsta.2021.0192, 2021.

Barkley, Z. R., Lauvaux, T., Davis, K. J., Deng, A., Miles, N. L., Richardson, S. J., Cao, Y., Sweeney, C., Karion, A., Smith, M., Kort, E. A., Schwietzke, S., Murphy, T., Cervone, G., Martins, D., and Maasakkers, J. D.: Improved Mechanistic Understanding of Natural Gas Methane Emissions from Spatially Resolved Aircraft Measurements, Environmental Science & Technology, 51, 7286–7294, https://doi.org/10.1021/acs.est.7b01810, 2017.

Barton-Grimley, R. A., Nehrir, A. R., Kooi, S. A., Collins, J. E., Harper, D. B., Notari, A., Lee, J., DiGangi, J. P., Choi, Y., and Davis, K. J.: Evaluation of the High Altitude Lidar Observatory (HALO) methane retrievals during the summer 2019 ACT-America campaign, Atmospheric measurement techniques, 15, 4623–4650, 2022.

Basso, L. S., Georgievski, G., Brovkin, V., Beer, C., Rödenbeck, C., and Göckede, M.: A top-down evaluation of bottom-up estimates to reduce uncertainty in methane emissions from Arctic wetlands, Biogeosciences, 23, 2815–2830, 2026.

Bastviken, D., Cole, J., Pace, M., and Tranvik, L.: Methane emissions from lakes: Dependence of lake characteristics, two regional assessments, and a global estimate, Global biogeochemical cycles, 18, 2004.

Bastviken, D., Tranvik, L. J., Downing, J. A., Crill, P. M., and Enrich-Prast, A.: Freshwater methane emissions offset the continental carbon sink, Science, 331, 50–50, 2011.

Belušić, D. and Mahrt, L.: Estimation of length scales from mesoscale networks, Tellus A: Dynamic Meteorology and Oceanography, 60, 706–715, 2008.

Bridgham, S. D., Cadillo-Quiroz, H., Keller, J. K., and Zhuang, Q.: Methane emissions from wetlands: biogeochemical, microbial, and modeling perspectives from local to global scales, Global change biology, 19, 1325–1346, 2013.

Briggs, G. A.: Diffusion estimation for small emissions, Atmospheric turbulence and diffusion laboratory, 965, 83–145, 1973.

Conley, S., Faloona, I., Mehrotra, S., Suard, M., Lenschow, D. H., Sweeney, C., Herndon, S., Schwietzke, S., Pétron, G., Pifer, J., Kort, E. A., and Schnell, R.: Application of Gauss's Theorem to quantify localized surface emissions from airborne measurements of wind and trace gases, Atmospheric Measurement Techniques, 10, 3345–3358, https://doi.org/10.5194/amt-10-3345-2017, 2017.

Desjardins, R., Worth, D., Pattey, E., VanderZaag, A., Srinivasan, R., Mauder, M., Worthy, D., Sweeney, C., and Metzger, S.: The challenge of reconciling bottom-up agricultural methane emissions inventories with top-down measurements, Agricultural and Forest Meteorology, 248, 48–59, 2018.

Elder, C. D., Thompson, D. R., Thorpe, A. K., Hanke, P., Walter Anthony, K. M., and Miller, C. E.: Airborne mapping reveals emergent power law of arctic methane emissions, Geophysical Research Letters, 47, e2019GL085 707, 2020.

https://doi.org/10.5194/egusphere-2026-3109
Preprint. Discussion started: 13 July 2026

Feron, S., Malhotra, A., Bansal, S., Fluet-Chouinard, E., McNicol, G., Knox, S. H., Delwiche, K. B., Cordero, R. R., Ouyang, Z., Zhang, Z., Poulter, B., and Jackson, R. B.: Recent increases in annual, seasonal, and extreme methane fluxes driven by changes in climate and vegetation in boreal and temperate wetland ecosystems, Global Change Biology, 30, e17 131, https://doi.org/10.1111/gcb.17131, 2024.

Forbrich, I., Yazbeck, T., Sulman, B., Morin, T. H., Tang, A. C. I., and Bohrer, G.: Three decades of wetland methane surface flux modeling by earth system models-advances, applications, and challenges, Journal of Geophysical Research: Biogeosciences, 129, e2023JG007 915, 2024.

France, J. L., Bateson, P., Dominutti, P., Allen, G., Andrews, S., Bauguitte, S., Coleman, M., Lachlan-Cope, T., Fisher, R. E., Huang, L., Jones, A. E., Lee, J., Lowry, D., Pitt, J., Purvis, R., Pyle, J., Shaw, J., Warwick, N., Weiss, A., Wilde, S., Witherstone, J., and Young, S.: Facility-level measurement of offshore oil and gas installations from a medium-sized airborne platform, Atmospheric Measurement Techniques, 14, 71–88, https://doi.org/10.5194/amt-14-71-2021, 2021.

Gifford Jr, F.: Statistical properties of a fluctuating plume dispersion model, in: Advances in geophysics, vol. 6, pp. 117–137, Elsevier, 1959.

Golder, D.: Relations among stability parameters in the surface layer, Boundary-Layer Meteorology, 3, 47–58, 1972.

He, K., Li, W., Zhang, Y., Zeng, A., de Graaf, I. E. M., Aguilos, M., Sun, G., McNulty, S. G., King, J. S., Flanagan, N. E., and Richardson, C. J.: Temperature and water levels collectively regulate methane emissions from subtropical freshwater wetlands, Global Biogeochemical Cycles, 39, e2024GB008 372, https://doi.org/10.1029/2024GB008372, 2025.

Helmig, D. and Caputi, D.: Top-down versus bottom-up atmospheric emission estimates from oil and natural gas operations, Earth' s Future, 13, e2025EF006 534, 2025.

Hristov, A. N., Kebreab, E., Niu, M., Oh, J., Bannink, A., Bayat, A. R., Boland, T. M., Brito, A. F., Casper, D. P., Crompton, L. A., Dijkstra, J., Eugène, M., Garnsworthy, P. C., Haque, N., Hellwing, A. L. F., Huhtanen, P., Kreuzer, M., Kuhla, B., Lund, P., Madsen, J., Martin, C., Moate, P. J., Muetzel, S., Muñoz, C., Peiren, N., Powell, J. M., Reynolds, C. K., Schwarm, A., Shingfield, K. J., Storlien, T. M., Weisbjerg, M. R., Yáñez-Ruiz, D. R., and Yu, Z.: Symposium review: Uncertainties in enteric methane inventories, measurement techniques, and prediction models, Journal of Dairy Science, 101, 6655–6674, https://doi.org/10.3168/jds.2017-13536, 2018.

Hutchinson, G. and Mosier, A.: Improved soil cover method for field measurement of nitrous oxide fluxes, Soil Science Society of America Journal, 45, 311–316, 1981.

Jin, L., Ghirardelli, M., Mann, J., Sjöholm, M., Kral, S. T., and Reuder, J.: Rotary-wing drone-induced flow–comparison of simulations with lidar measurements, Atmospheric Measurement Techniques, 17, 2721–2737, 2024.

Kirschke, S., Bousquet, P., Ciais, P., Saunois, M., Canadell, J. G., Dlugokencky, E. J., Bergamaschi, P., Bergmann, D., Blake, D. R., Bruhwiler, L., Cameron-Smith, P., Castaldi, S., Chevallier, F., Feng, L., Fraser, A., Heimann, M., Hodson, E. L., Houweling, S., Josse, B., Fraser, P. J., Krummel, P. B., Lamarque, J.-F., Langenfelds, R. L., Le Quéré, C., Naik, V., O' Doherty, S., Palmer, P. I., Pison, I., Plummer, D., Poulter, B., Prinn, R. G., Rigby, M., Ringeval, B., Santini, M., Schmidt, M., Shindell, D. T., Simpson, I. J., Spahni, R., Steele, L. P., Strode, S. A., Sudo, K., Szopa, S., van der Werf, G. R., Voulgarakis, A., van Weele, M., Weiss, R. F., Williams, J. E., and Zeng, G.: Three decades of global methane sources and sinks, Nature Geoscience, 6, 813–823, https://doi.org/10.1038/ngeo1955, 2013.

Köster, E., Köster, K., Berninger, F., Aaltonen, H., Zhou, X., and Pumpanen, J.: Carbon dioxide, methane and nitrous oxide fluxes from a fire chronosequence in subarctic boreal forests of Canada, Science of the total environment, 601, 895–905, 2017.

Kyzivat, E. D., Smith, L. C., Garcia-Tigreros, F., Huang, C., Wang, C., Langhorst, T., Fayne, J. V., Harlan, M. E., Ishitsuka, Y., Feng, D., Dolan, W., Pitcher, L. H., Wickland, K. P., Dornblaser, M. M., Striegl, R. G., Pavelsky, T. M., Butman, D. E., and Gleason, C. J.: The importance of lake emergent aquatic vegetation for estimating Arctic-boreal methane emissions, Journal of Geophysical Research: Biogeosciences, 127, e2021JG006 635, https://doi.org/10.1029/2021JG006635, 2022.

https://doi.org/10.5194/egusphere-2026-3109
Preprint. Discussion started: 13 July 2026

Lan, X., Nisbet, E. G., Dlugokencky, E. J., and Michel, S. E.: What do we know about the global methane budget? Results from four decades of atmospheric CH4 observations and the way forward, Philosophical Transactions of the Royal Society A: Mathematical, Physical and Engineering Sciences, 379, 2021.

Lehner, B. and Döll, P.: Development and validation of a global database of lakes, reservoirs and wetlands, Journal of hydrology, 296, 1–22, 2004.

Mahrt, L.: Stratified atmospheric boundary layers, Boundary-Layer Meteorology, 90, 375–396, 1999.

Maier, M. and Schack-Kirchner, H.: Using the gradient method to determine soil gas flux: A review, Agricultural and forest meteorology, 192, 78–95, 2014.

Malone, S., Oh, Y., Arndt, K., Burba, G., Commane, R., Contosta, A., Goodrich, J., Loescher, H., Starr, G., and Varner, R.: Gaps in Network Infrastructure limit our understanding of biogenic methane emissions in the United States, Biogeosciences Discussions, 2021, 1–24, 2021.

Martinez, B., Miller, T. W., and Yalin, A. P.: Cavity ring-down methane sensor for small unmanned aerial systems, Sensors, 20, 454, 2020.

Masson-Delmotte, V., Zhai, P., Pirani, A., Connors, S., Péan, C., Berger, S., Caud, N., Chen, Y., Goldfarb, L., Gomis, M., Huang, M., Leitzell, K., Lonnoy, E., Matthews, J., Maycock, T., Waterfield, T., Yelek cci, O., Yu, R., and Zhou, B.: Climate Change 2021: The Physical Science Basis. Contribution of Working Group I to the Sixth Assessment Report of the Intergovernmental Panel on Climate Change, Cambridge University Press, https://doi.org/10.1017/9781009157896, 2021.

Matthes, J. H., Sturtevant, C., Verfaillie, J., Knox, S., and Baldocchi, D.: Parsing the variability in CH4 flux at a spatially heterogeneous wetland: Integrating multiple eddy covariance towers with high-resolution flux footprint analysis, Journal of Geophysical Research: Biogeosciences, 119, 1322–1339, 2014.

Metzger, S.: Surface-atmosphere exchange in a box: Making the control volume a suitable representation for in-situ observations, Agricultural and Forest Meteorology, 255, 68–80, 2018.

Mohammadloo, T. H., Jones, M., van de Kerkhof, B., Dawson, K., Smith, B. J., Conley, S., Corbett, A., and IJzermans, R.: Quantitative estimate of several sources of uncertainty in drone-based methane emission measurements, Atmospheric Measurement Techniques, 18, 1301–1324, 2025.

Monin, A. S. and Obukhov, A. M.: Basic laws of turbulent mixing in the surface layer of the atmosphere, Contributions of the Geophysical Institute of the Academy of Sciences of the USSR, 151, 163–187, 1954.

Mylne, K. R. and Mason, P.: Concentration fluctuation measurements in a dispersing plume at a range of up to 1000 m, Quarterly Journal of the Royal Meteorological Society, 117, 177–206, 1991.

Olefeldt, D., Heffernan, L., Jones, M. C., Sannel, A. B. K., Treat, C. C., and Turetsky, M. R.: Permafrost thaw in northern peatlands: rapid changes in ecosystem and landscape functions, Ecosystem collapse and climate change, pp. 27–67, 2021.

Ortiz-Llorente, M. J. and Alvarez-Cobelas, M.: Comparison of biogenic methane emissions from unmanaged estuaries, lakes, oceans, rivers and wetlands, Atmospheric Environment, 59, 328–337, 2012.

Pasquill, F. and Smith, F. B.: Atmospheric diffusion, vol. 437, Ellis Horwood Chichester, 1983.

Pastorello, G., Trotta, C., Canfora, E., Chu, H., Christianson, D., Cheah, Y.-W., Poindexter, C., Chen, J., Elbashandy, A., Humphrey, M., et al.: The FLUXNET2015 dataset and the ONEFlux processing pipeline for eddy covariance data, Scientific Data, 7, 225, https://doi.org/10.1038/s41597-020-0534-3, 2020.

Praetzel, L. S. E., Schmiedeskamp, M., and Knorr, K.-H.: Temperature and sediment properties drive spatiotemporal variability of methane ebullition in a small and shallow temperate lake, Limnology and Oceanography, 66, 2598–2610, 2021.

https://doi.org/10.5194/egusphere-2026-3109
Preprint. Discussion started: 13 July 2026

Räsänen, A., Manninen, T., Korkiakoski, M., Lohila, A., and Virtanen, T.: Predicting catchment-scale methane fluxes with multi-source remote sensing, Landscape Ecology, 36, 1177–1195, 2021.

Ražnjević, A., Van Heerwaarden, C., and Krol, M.: Evaluation of two common source estimation measurement strategies using large-eddy simulation of plume dispersion under neutral atmospheric conditions, Atmospheric Measurement Techniques Discussions, 2022, 1–27, 2022.

Rey-Sanchez, C., Bohrer, G., Slater, J., Li, Y.-F., Grau-Andrés, R., Hao, Y., Rich, V. I., and Davies, G. M.: The ratio of methanogens to methanotrophs and water-level dynamics drive methane transfer velocity in a temperate kettle-hole peat bog, Biogeosciences, 16, 3207–3231, 2019.

Riquelme del Rio, B., Sepulveda-Jauregui, A., Salas-Rabaza, J. A., Mackenzie, R., and Thalasso, F.: Fine-scale spatial variability of greenhouse gas emissions from a subantarctic peatland bog, Environmental Science & Technology, 58, 7393–7402, 2024.

Rodríguez-García, V. G., Palma-Gallardo, L. O., Silva-Olmedo, F., and Thalasso, F.: A simple and low-cost open dynamic chamber for the versatile determination of methane emissions from aquatic surfaces, Limnology and Oceanography: Methods, 21, 828–836, 2023.

Rozmiarek, K. S., Yang, J., Schambach, J., Bennett, H., Caro, T. A., Sammon, J., Whiting, J. J., Miller, P. R., Ricken, B., Bigler, L., Jayne, R. S., Fukuyama, D., Jones, T. R., and Smallwood, C. R.: Methane hotspot dynamics in thermokarst soils: microbial volatile organic compounds, isotopic signatures, and metagenomics in a thawing permafrost system at Big Trail Lake, Alaska, Frontiers in Microbiology, 16, 1657 143, https://doi.org/10.3389/fmicb.2025.1657143, 2025.

Saunois, M., Martinez, A., Poulter, B., Zhang, Z., Raymond, P. A., Regnier, P., Canadell, J. G., Jackson, R. B., Patra, P. K., Bousquet, P., Ciais, P., Dlugokencky, E. J., Lan, X., Allen, G. H., Bastviken, D., Beerling, D. J., Belikov, D. A., Blake, D. R., Castaldi, S., Crippa, M., Deemer, B. R., Dennison, F., Etiope, G., Gedney, N., Höglund-Isaksson, L., Holgerson, M. A., Hopcroft, P. O., Hugelius, G., Ito, A., Jain, A. K., Janardanan, R., Johnson, M. S., Kleinen, T., Krummel, P. B., Lauerwald, R., Li, T., Liu, X., McDonald, K. C., Melton, J. R., Mühle, J., Müller, J., Murguia-Flores, F., Niwa, Y., Noce, S., Pan, S., Parker, R. J., Peng, C., Ramonet, M., Riley, W. J., Rocher-Ros, G., Rosentreter, J. A., Sasakawa, M., Segers, A., Smith, S. J., Stanley, E. H., Thanwerdas, J., Tian, H., Tsuruta, A., Tubiello, F. N., Weber, T. S., van der Werf, G. R., Worthy, D. E. J., Xi, Y., Yoshida, Y., Zhang, W., Zheng, B., Zhu, Q., Zhu, Q., and Zhuang, Q.: Global Methane Budget 2000–2020, Earth System Science Data, 17, 1873–1958, https://doi.org/10.5194/essd-17-1873-2025, 2025.

Shah, A., Pitt, J., Kabbabe, K., and Allen, G.: Suitability of a non-dispersive infrared methane sensor package for flux quantification using an unmanned aerial vehicle, Sensors, 19, 4705, 2019.

Shaw, J. T., Shah, A., Yong, H., and Allen, G.: Methods for quantifying methane emissions using unmanned aerial vehicles: A review, Philosophical Transactions of the Royal Society A: Mathematical, Physical and Engineering Sciences, 379, 2021.

Sieczko, A. K., Duc, N. T., Schenk, J., Pajala, G., Rudberg, D., Sawakuchi, H. O., and Bastviken, D.: Diel variability of methane emissions from lakes, Proceedings of the National Academy of Sciences, 117, 21 488–21 494, 2020.

Stull, R. B.: An introduction to boundary layer meteorology, Springer Science & Business Media, 2012.

Tanentzap, A. J., Woodman, S. G., Kolmakova, O., and Zhang, Y.: Sediment Chemistry Predicts Littoral Methane Emissions, Ecosystems, 29, 31, 2026.

Thielicke, W., Hübert, W., Müller, U., Eggert, M., and Wilhelm, P.: Towards accurate and practical drone-based wind measurements with an ultrasonic anemometer, Atmospheric Measurement Techniques, 14, 1303–1318, 2021.

Turner, D. B.: Workbook of atmospheric dispersion estimates: an introduction to dispersion modeling, CRC press, 2020.

Warhaft, Z.: Passive scalars in turbulent flows, Annual review of fluid mechanics, 32, 203–240, 2000.

https://doi.org/10.5194/egusphere-2026-3109
Preprint. Discussion started: 13 July 2026

Wik, M., Varner, R. K., Anthony, K. W., MacIntyre, S., and Bastviken, D.: Climate-sensitive northern lakes and ponds are critical components of methane release, Nature Geoscience, 9, 99–105, 2016.

Yvon-Durocher, G., Allen, A. P., Bastviken, D., Conrad, R., Gudasz, C., St-Pierre, A., Thanh-Duc, N., and Del Giorgio, P. A.: Methane fluxes show consistent temperature dependence across microbial to ecosystem scales, Nature, 507, 488–491, 2014.

Zhu, Q., Jacob, D. J., Yuan, K., Li, F., Runkle, B. R. K., Chen, M., Bloom, A. A., Poulter, B., East, J. D., Riley, W. J., McNicol, G., Worden, J., Frankenberg, C., and Halabisky, M.: Advancements and opportunities to improve bottom–up estimates of global wetland methane emissions, Environmental Research Letters, 20, 023 001, https://doi.org/10.1088/1748-9326/adad02, 2025.